Accepted Manuscript

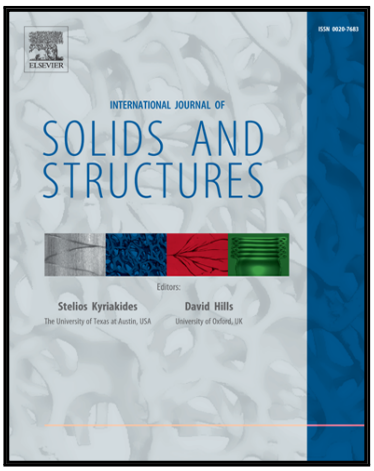

Dynamic contact in multiferroic energy conversion

Xin Zhang , Zhanjiang Wang , Huoming Shen , Q. Jane Wang

PII: S0020-7683(18)30090-8
DOI: 10.1016/j.ijsolstr.2018.02.034
Reference: SAS 9922

To appear in: *International Journal of Solids and Structures*

Received date: 3 December 2017
Revised date: 6 February 2018
Accepted date: 26 February 2018

Please cite this article as: Xin Zhang , Zhanjiang Wang , Huoming Shen , Q. Jane Wang , Dynamic contact in multiferroic energy conversion, *International Journal of Solids and Structures* (2018), doi: 10.1016/j.ijsolstr.2018.02.034

This is a PDF file of an unedited manuscript that has been accepted for publication. As a service to our customers we are providing this early version of the manuscript. The manuscript will undergo copyediting, typesetting, and review of the resulting proof before it is published in its final form. Please note that during the production process errors may be discovered which could affect the content, and all legal disclaimers that apply to the journal pertain.

ACCEPTED MANUSCRIPT

Dynamic contact in multiferroic energy conversion

Xin Zhang [a, b], Zhanjiang Wang [c], Huoming Shen [a], Q. Jane Wang [b, c, *]

[a] School of Mechanics and Engineering, Southwest Jiaotong University, Chengdu 610031, China
[b] Department of Mechanical Engineering, Northwestern University, Evanston, IL 60208, USA
[c] Tribology Research Institute, Traction Power State Key Laboratory, Southwest Jiaotong University, Chengdu 610031, China

*Corresponding author: Q. Jane Wang, E-mail: qwang@northwestern.edu

Abstract

This paper reports a semi-analytical model (SAM) for simulating the dynamic contact of a rigid sphere and the surface of a multiferroic magnetoelectroelastic (MEE) film under an increasing applied force. The frequency response functions (FRFs) and their conversion into influence coefficients (ICs) for the MEE film are analytically derived, incorporating the loading velocity in a dynamic process. Fast numerical techniques, including the conjugate gradient method (CGM) and the fast Fourier transform (FFT), are employed for efficient numerical solutions to the dynamic contact behaviors, including the distributions and variations of contact pressure and electric/magnetic potentials, as well as subsurface stresses. The proposed model is implemented to analyze the influences of loading velocity, film thickness, and sphere radius on the dynamic MEE responses, including pressure/stresses and electric/magnetic potentials. An energy conversion factor is selected to evaluate the performance of MEE energy conversion. Furthermore, a sensitivity analysis is conducted to evaluate the influence of material properties and their coupling on the efficiency of mechanical-electric/magnetic energy conversion.

Key words: Multiferroic film, energy conversion, semi-analytical modeling, dynamic contact.

ACCEPTED MANUSCRIPT

Nomenclature

a^t acceleration of the rigid sphere at time t

a_0 contact radius in multiferroic half-space, m

A_k, $\bar{A}_k$ unknowns in potential functions

A_{ij} cofactors of matrix $[D]$

B_i magnetic induction along the x_i direction, N/(Am)

c relative moving velocity of the rigid sphere

c_{sw} shear wave velocity in the MEE film

c_{ijkl} elastic stiffness tensor, 10^9N/m^2

C^u, C^φ, C^ψ, C influence coefficients

d_{kij} piezomagnetic stiffness tensor, N/(Am)

$[D]$ a matrix

D_i electric displacement, C/m^2

e_{kij} piezoelectric stiffness tensor, C/m^2

f selected material constant

f^0 reference value for f

F displacement function

g surface magnetic charge,

g_z gap between two surfaces, m

g_{ij} electromagnetic coefficient, C/(Am)

G^u, G^φ, G^ψ frequency response functions

G displacement function

h_0 initial separation between two surfaces, m

h_t film thickness, m

H displacement function

i imaginary unit

m, n Fourier-transformed variables with respect to x_1, x_2 directions, respectively

M, N mesh numbers along the x_1, x_2 directions

M_e, N_e refined mesh numbers

M_s mass of the sphere

q surface electric charge,

p pressure, Pa

P applied force, N

P_0 referenced force, N

R radius of a spherical punch, m

R_0 referenced sphere radius, m

s_j variables relating to material properties

t loading time

T_{total} total time for one loading cycle

ACCEPTED MANUSCRIPT

u_i displacements along the x_i direction, m
V_0 maximum value of the loading velocity
V loading velocity of the sphere, m/s
W^P work by the applied force
x_j, X_j Cartesian coordinates in the spatial domain
F_s shape function

Greek letters
α distance of a node, (m, n), to the origin of the frequency domain
γ refinement level
$\kappa_{\alpha\beta}$ surface curvature tensor with $\kappa_{\alpha\beta} = -u_{i,\alpha\beta}$
δ^t indentation depth at time t
ε_{ij} dielectric permittivity, $10^{-9}C^2/(Nm^2)$
μ_{ij} magnetic permeability, $10^{-6}Ns^2/C^2$
σ_{ij} stress components, Pa
σ_s von Mises stress, Pa
ρ mass density
η_P energy conversion factor
ϕ electric potential, V
φ magnetic potential, A
ψ_i harmonic functions
Γ_c contact zone
Γ surface energy density
Π^S strain energy
Π^E electric energy
Π^M magnetic energy
Π^{PE} piezoelectric energy
Π^{PM} piezomagnetic energy
Π^{ME} magnetoelectric energy
Δ_{xi} grid size in the x_i directions, m

Special marks
$\approx$ double continuous Fourier transform
^ discrete Fourier transform
$|\cdot|$ determinant of a matrix
IFFT inverse fast Fourier transform

ACCEPTED MANUSCRIPT

ACCEPTED MANUSCRIPT

1. Introduction

Multiferroic materials are noteworthy for their strong coupling of ferroelectricity, ferromagnetism, and ferroelasticity (Eerenstein et al., 2006; Wang et al., 2010). A large amount of research has been conducted to explore methods for synthesizing and characterizing multiferroics, aiming to achieve a larger magnetoelectroelastic (MEE) coupling effect (Liu et al., 2010; Ramesh and Spaldin, 2007). Most recent studies on multiferroics reported truly remarkable MEE coupling effects (Kirchhof et al., 2013; Kulkarni et al., 2014), which promote the applications of these materials in AC/DC magnetic field sensors, photovoltaic multiferroic solar cells, multiferroic gyrators, and energy harvesting multiferroics (Vopson, 2015). Among these applications, the devices capable of harvesting energy from environmental sources (e.g. air flow, body movements, hydraulic pressure, and ambient vibrations) are of huge commercial values due to their suitability to self-powered systems in portable electronics, environmental condition monitors, structural health monitors, and medical implants (Vopson, 2015; Zhou et al., 2016). Although current energy harvesting devices are mainly based on piezoelectric semiconductors, known as piezoelectric nanogenerators (NGs) (Hu and Wang, 2015; Kim et al., 2014; Wang et al., 2014; Wang and Song, 2006), other approaches for energy harvest based on magnetostrictive materials have been reported in (Erturk et al., 2009; Wang and Yuan, 2008; Zucca et al., 2011). Foreseeably, multiferroic devices combining the piezoelectric and magnetostrictive advantages could result in promising energy harvesters with ultra-high efficiency, as reported in (Challa et al., 2009; Lafont et al., 2012; Li et al., 2015a; Shan et al., 2013).

Device development requires systematic optimization for the efficiency of energy conversion and durability of operation, which should be built on deep understanding of the material performance. Recently, a great deal of research on the piezoelectric and magnetostrictive energy harvesters has been conducted for the energy conversion maximization. Several examples are the work by Gu et al. (2012) on structural optimization for flexible fiber energy harvesters, the study by Xu and Qin (2017) about the external force optimization for piezoelectric energy harvesters, the research by Sun and Kim (2010) on the topology optimization for MEE laminate composites, and the optimization by Loja et al. (2014) for several MEE composite structures utilizing differential evolution. However, these works were mainly focused on a static analysis of the piezoelectric or MEE materials, as well as a simplified treatment of the fully coupled piezoelectric/MEE problems. A comprehensive investigation of the dynamic behaviors of multiferroic materials is the first step towards in-depth understanding of the overall responses of the MEE energy conversion. Considering multiferroic materials, mainly in the form of a thin film bonded to a substrate, a thin-film-based model is a natural choice for MEE dynamics, where the MEE film can be described as a voltage source for utilizing the electric potential to drive the electron flow

ACCEPTED MANUSCRIPT

through the circuit. In order to determine the dynamic characteristics of a MEE film, the voltage source's voltage dependence on the applied force and loading velocity should be analyzed firstly, for which several key issues should be addressed: (a) what are the key dynamic characteristics of a MEE thin-film subjected to dynamic contact loading? (b) How does the loading velocity affect the mechanical and electric/magnetic responses? (c) What is the general role of MEE coupling in a contact process for energy conversion? However, the dynamic analysis of a contact process involves complicated field coupling and strong nonlinearity; it requires a huge amount of computation; therefore, an efficient method is highly demanded.

Many researchers have investigated the static contact behaviors of MEE coupling. Several examples are the analytical works by Hou et al. (2003) and Chen et al. (2010) on the frictionless contact involving a MEE half-space, the analytical study and numerical implementation by Zhou and Lee (2013) on the frictional contact involving a MEE half-plane, the numerical modeling by Michopoulos et al. (2015) on the contact behaviors of MEE half-space based on the finite element method (FEM), the investigation of Rodríguez-Tembleque et al. (2016a) on the frictional contact of a MEE half-space using the boundary element method (BEM), and the simulation by Zhang et al. (2018) on the frictional contact of two MEE bodies using the semi-analytical modeling (SAM) approach. However, little work has been done for MEE films, although many investigated the static indentation responses of piezoelectric films by analytical approaches (Wang and Chen, 2011; Wang et al., 2008), by using the FEM (Liu and Yang, 2012) and the BEM (Rodríguez-Tembleque et al., 2016b), and MEE films by using SAM (Zhang et al., 2017). Furthermore, the dynamic contact analysis of MEE films is largely missing due to the complexity of MEE coupling in a multiferroic film, which makes it difficult to obtain exact analytical solutions. The work reported in this paper intends to develop the solution for dynamic contact of MEE films and explore an efficient model for tackling the dynamic contact responses of MEE films.

Semi-analytical modeling (SAM) (Liu et al., 2000; Polonsky and Keer, 1999; Webster and Sayles, 1986), built upon core analytical solutions and supported by fast numerical techniques, has been proven to be efficient for solving three-dimensional (3D) contact problems involving layered materials (Wang et al., 2011; Wang et al., 2015; Yu et al., 2014), or materials with contact elastic–plasticity (Liu et al., 2012; Wang et al., 2013), even subjected to fretting (Zhang et al., 2015; Zhou et al., 2017). The core analytical solutions to displacements, electric/magnetic potentials, stresses, electric displacements, and magnetic inductions of the MEE film should be derived first pertaining to a set of generalized normal force, surface electric charge, and surface magnetic charge, together with incorporation of the loading velocity in a dynamic process. Recently, Zhou and Lee (2012a), and Zhou and Kim

(2015) studied the exact contact problem between the MEE half-plane and a moving punch, which inspired our current study on deriving the core analytical solutions of 3D dynamic contacts of MEE films. Then fast numerical techniques, such as the conjugate gradient method (CGM) and the fast Fourier transform (FFT), can be incorporated for efficient numerical results to the dynamic contact behaviors, including the distributions of contact pressure and electric/magnetic potentials, as well as subsurface stresses. The proposed model is verified by comparing the results from its degenerated forms with analytical solutions for a MEE half-space and the corresponding numerical results for selected static contact of MEE films. The model is further used to study general MEE transient behaviors. Thus, the general role of the MEE coupling in a dynamic contact process is explored and the dynamic contact mechanism in multiferroic energy conversion can be revealed.

2. Formulation

2.1 Problem description

Figure 1 (a) shows the working mechanism of a magnetoelectroelastic (MEE) energy converter, where the rigid sphere of radius *R* represents any indenter whose tip geometry can be modeled by its local curvature, which is on the top surface of a transversely isotropic multiferroic MEE film under an increasing applied force $P(t)$ along the z axis. The lower surface of the film of finite thickness h_t is perfectly bonded to a rigid grounded substrate. The rectangular coordinates (x, y, z) are introduced here with the x-y plane parallel to the plane of isotropy of the multiferroic film. There are two solution routes for the presented problem: a) the applied force $P(t)$ on the rigid sphere is given as a function of time t. Based on $P(t)$ at each time step t, the contact problem can be solved to obtain the indentation depth, δ, contact pressure, and surface electric/magnetic potential, etc.; b) the loading velocity $V(t)$ of the rigid sphere is given at each time step t as a given input, which can be employed to further determine the indentation depth δ. Then the contact problem is naturally solved to obtain the applied force, contact pressure, and surface electric/magnetic potentials, etc. In route a), the increasing applied force $P(t)$ is generally assumed as a harmonic excitation. The influence of the applied force, in different variation shapes, on the piezoelectric behavior has been studied in (Xu and Qin, 2017). However, the loading velocity also affected the piezoelectric/MEE behaviors. In route b), the shape of the loading velocity variation appears as an input in the current study, instead of the force variation shape, which offers a convenient way to further study the dynamic coupling behaviors of MEE films in multiferroic energy conversion.

The dynamic loading velocity, $V(t)$, of the rigid sphere can be prescribed in two typical forms: (i) a triangular shape and (ii) a sinusoidal shape, as shown in insets (i) and (ii) of Fig. 1 (a). The electrical characteristics of the velocity-induced MEE converter can be described as a simple resistor-capacitor (RC) equivalent circuit, as shown in Fig. 1 (b), where

R_{Ex} is an external load resistor, R_{In} is the internal resistance of the MEE converter, C_{MEE} is the capacitance of the converter. The performance of the MEE film can be described as voltage source V_{MEE}, and capacitance C_{MEE} together with an internal resistance R_{In}, which utilizes the electric potential to drive the electron flow through the circuit.

At time step t, the dynamic contact between the sphere and the MEE film can be subjected to an increasing applied force P and a certain velocity V. Contact modeling is required to obtain the output parameters based on the input information, as shown in Fig. 1 (c). To this end, the theoretical expressions for dynamic MEE coupling can be derived by incorporating velocity V in a dynamic process, which are then employed for developing efficient numerical solutions to the dynamic contact problem.

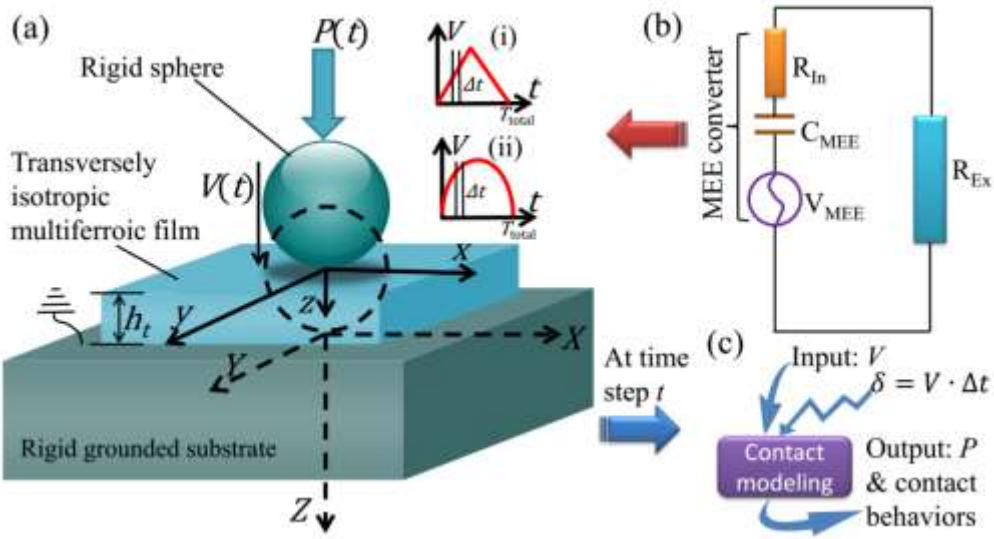

Fig. 1. Illustration of the working mechanism of a transversely isotropic multiferroic MEE energy converter.

2.2 Basic equations and boundary conditions

The constitutive relations for MEE films are given by (Hou et al. 2003; Chen et al. 2010)

$$\begin{aligned} \sigma_{ij} &= c_{ijkl}\gamma_{kl} - e_{kij}E_k - d_{kij}H_k, \\ D_i &= e_{ikl}\gamma_{kl} + \varepsilon_{ij}E_j + g_{ij}H_j, \\ B_i &= d_{ikl}\gamma_{kl} + g_{ij}E_j + \mu_{ij}H_j, \end{aligned} \tag{1}$$

with

$$\begin{aligned} \gamma_{ij} &= \frac{1}{2}(u_{i,j} + u_{j,i}), \\ E_i &= -\phi_{,i}, \\ H_i &= -\varphi_{,i}, \end{aligned} \tag{2}$$

where σ_{ij}, D_i and B_i are the elastic stress tensor, electric displacement vector, and magnetic

induction vector; c_{ij}, e_{ij} and d_{ij} denote the elastic moduli, piezoelectric coefficients, and piezomagnetic coefficients; ε_{ij}, g_{ij} and μ_{ij} represent the dielectric permittivity, electromagnetic coefficients, and magnetic permeability, respectively; γ_{ij}, E_i and H_i are the elastic strain tensor, electric field vector, and magnetic field vector; u_i, ϕ and φ are the elastic displacement vector, electric potential, and magnetic potential. Here and throughout this paper, the standard index notation is used, where comma represents differentiation with respect to the suffix coordinate. For clarity, the Einstein summation convention for repeated indices is used.

For typical MEE materials, the characteristic frequencies for elastic and electromagnetic processes are about 10^4 Hz and 10^7 Hz, respectively. In the presence of transient loadings, the changes in the electromagnetic fields in the MEE body are assumed to be immediate, in which the electromagnetic field can be regarded as a quasi-static state (Bonaldi et al., 2015; Parton and Kudryavtsev, 1988; Sladek et al., 2010). Therefore in absence of body sources, the equilibrium equations and the Maxwell equations are

$$\begin{aligned} &\sigma_{ij,i} = \rho \frac{\partial^2 u_i}{\partial t^2}, \\ &D_{i,i} = 0, \\ &B_{i,i} = 0, \end{aligned} \tag{3}$$

where ρ is the mass density and t represents time.

The boundary conditions at the upper surface of the MEE film can be written as

$$\begin{aligned} &\sigma_{xz}\big|_{z=0} = 0, \\ &\sigma_{yz}\big|_{z=0} = 0, \\ &\sigma_{zz}\big|_{z=0} = -p, \\ &D_z\big|_{z=0} = -q, \\ &B_z\big|_{z=0} = -g, \end{aligned} \tag{4}$$

where p, q and g represent pressure, surface electric charge, and surface magnetic charge, respectively.

Because the lower surface of the film is perfectly bonded to a rigid grounded substrate, the boundary conditions at the lower surface are

$$
\begin{aligned}
&u_x\big|_{z=h_t} = 0,\\
&u_y\big|_{z=h_t} = 0,\\
&u_z\big|_{z=h_t} = 0,\\
&\phi\big|_{z=h_t} = 0,\\
&\varphi\big|_{z=h_t} = 0.
\end{aligned}
\tag{5}
$$

In the context of transversely isotropic MEE media, substituting Eq. (3) into Eq. (1) leads to the following governing equations,

$$
\begin{aligned}
&(c_{11}\frac{\partial^2}{\partial x^2}+c_{66}\frac{\partial^2}{\partial y^2}+c_{44}\frac{\partial^2}{\partial z^2})u_x+(c_{12}+c_{66})\frac{\partial^2 u_y}{\partial x\partial y}+(c_{13}+c_{44})\frac{\partial^2 u_z}{\partial x\partial z}\\
&+(e_{31}+e_{15})\frac{\partial^2\phi}{\partial x\partial z}+(d_{31}+d_{15})\frac{\partial^2\varphi}{\partial x\partial z}=\rho\frac{\partial^2 u_x}{\partial t^2},
\end{aligned}
\tag{6}
$$

$$
\begin{aligned}
&(c_{12}+c_{66})\frac{\partial^2 u_x}{\partial x\partial y}+(c_{66}\frac{\partial^2}{\partial x^2}+c_{11}\frac{\partial^2}{\partial y^2}+c_{44}\frac{\partial^2}{\partial z^2})u_y+(c_{13}+c_{44})\frac{\partial^2 u_z}{\partial y\partial z}\\
&+(e_{15}+e_{31})\frac{\partial^2\phi}{\partial y\partial z}+(d_{15}+d_{31})\frac{\partial^2\varphi}{\partial y\partial z}=\rho\frac{\partial^2 u_y}{\partial t^2},
\end{aligned}
\tag{7}
$$

$$
\begin{aligned}
&(c_{13}+c_{44})(\frac{\partial^2 u_x}{\partial x\partial z}+\frac{\partial^2 u_y}{\partial y\partial z})+(c_{44}\frac{\partial^2}{\partial x^2}+c_{44}\frac{\partial^2}{\partial y^2}+c_{33}\frac{\partial^2}{\partial z^2})u_z+(e_{15}\frac{\partial^2}{\partial x^2}\\
&+e_{15}\frac{\partial^2}{\partial y^2}+e_{33}\frac{\partial^2}{\partial z^2})\phi+(d_{15}\frac{\partial^2}{\partial x^2}+d_{15}\frac{\partial^2}{\partial y^2}+d_{33}\frac{\partial^2}{\partial z^2})\varphi=\rho\frac{\partial^2 u_z}{\partial t^2},
\end{aligned}
\tag{8}
$$

$$
\begin{aligned}
&(e_{15}+e_{31})(\frac{\partial^2 u_x}{\partial x\partial z}+\frac{\partial^2 u_y}{\partial y\partial z})+(e_{15}\frac{\partial^2}{\partial x^2}+e_{15}\frac{\partial^2}{\partial y^2}+e_{33}\frac{\partial^2}{\partial z^2})u_z-(\varepsilon_{11}\frac{\partial^2}{\partial x^2}\\
&+\varepsilon_{11}\frac{\partial^2}{\partial y^2}+\varepsilon_{33}\frac{\partial^2}{\partial z^2})\phi-(g_{11}\frac{\partial^2}{\partial x^2}+g_{11}\frac{\partial^2}{\partial y^2}+g_{33}\frac{\partial^2}{\partial z^2})\varphi=0,
\end{aligned}
\tag{9}
$$

$$
\begin{aligned}
&(d_{15}+d_{31})(\frac{\partial^2 u_x}{\partial x\partial z}+\frac{\partial^2 u_y}{\partial y\partial z})+(d_{15}\frac{\partial^2}{\partial x^2}+d_{15}\frac{\partial^2}{\partial y^2}+d_{33}\frac{\partial^2}{\partial z^2})u_z-(g_{11}\frac{\partial^2}{\partial x^2}\\
&+g_{11}\frac{\partial^2}{\partial y^2}+g_{33}\frac{\partial^2}{\partial z^2})\phi-(\mu_{11}\frac{\partial^2}{\partial x^2}+\mu_{11}\frac{\partial^2}{\partial y^2}+\mu_{33}\frac{\partial^2}{\partial z^2})\varphi=0.
\end{aligned}
\tag{10}
$$

The Galilean transform is introduced to connect coordinates systems (*x, y, z*) and *(X, Y, Z)* (Zhou and Lee, 2012a), shown as follows

$$
X = x,\ Y = y,\ Z = z - Vt, \tag{11}
$$

with

$$\frac{\partial}{\partial X}=\frac{\partial}{\partial x},\ \frac{\partial}{\partial Y}=\frac{\partial}{\partial y},\ \frac{\partial}{\partial Z}=\frac{\partial}{\partial z},\ \frac{\partial}{\partial t}=-V\frac{\partial}{\partial Z}. \tag{12}$$

Denote $c = V/c_{sw}$ as the relative moving velocity of the rigid sphere, where $c_{sw} = \sqrt{c_{44}/\rho}$ is the shear wave velocity in the MEE film. Substituting Eq. (11) into Eqs. (6-10) leads to the following,

$$\begin{aligned}&[c_{11}\frac{\partial^2}{\partial X^2}+c_{66}\frac{\partial^2}{\partial Y^2}+c_{44}(1-c^2)\frac{\partial^2}{\partial Z^2}]u_x+(c_{12}+c_{66})\frac{\partial^2 u_y}{\partial X\partial Y}+(c_{13}+c_{44})\frac{\partial^2 u_z}{\partial X\partial Z}\\&+(e_{31}+e_{15})\frac{\partial^2\phi}{\partial X\partial Z}+(d_{31}+d_{15})\frac{\partial^2\varphi}{\partial X\partial Z}=0,\end{aligned} \tag{13}$$

$$\begin{aligned}&(c_{12}+c_{66})\frac{\partial^2 u_x}{\partial X\partial Y}+[c_{66}\frac{\partial^2}{\partial X^2}+c_{11}\frac{\partial^2}{\partial Y^2}+c_{44}(1-c^2)\frac{\partial^2}{\partial Z^2}]u_y+(c_{13}+c_{44})\frac{\partial^2 u_z}{\partial Y\partial Z}\\&+(e_{15}+e_{31})\frac{\partial^2\phi}{\partial Y\partial Z}+(d_{15}+d_{31})\frac{\partial^2\varphi}{\partial Y\partial Z}=0,\end{aligned} \tag{14}$$

$$\begin{aligned}&(c_{13}+c_{44})(\frac{\partial^2 u_x}{\partial X\partial Z}+\frac{\partial^2 u_y}{\partial Y\partial Z})+[c_{44}\frac{\partial^2}{\partial X^2}+c_{44}\frac{\partial^2}{\partial Y^2}+(c_{33}-c_{44}c^2)\frac{\partial^2}{\partial Z^2}]u_z+(e_{15}\frac{\partial^2}{\partial X^2}\\&+e_{15}\frac{\partial^2}{\partial Y^2}+e_{33}\frac{\partial^2}{\partial Z^2})\phi+(d_{15}\frac{\partial^2}{\partial X^2}+d_{15}\frac{\partial^2}{\partial Y^2}+d_{33}\frac{\partial^2}{\partial Z^2})\varphi=0,\end{aligned} \tag{15}$$

$$\begin{aligned}&(e_{15}+e_{31})(\frac{\partial^2 u_x}{\partial X\partial Z}+\frac{\partial^2 u_y}{\partial Y\partial Z})+(e_{15}\frac{\partial^2}{\partial X^2}+e_{15}\frac{\partial^2}{\partial Y^2}+e_{33}\frac{\partial^2}{\partial Z^2})u_z-(\varepsilon_{11}\frac{\partial^2}{\partial X^2}\\&+\varepsilon_{11}\frac{\partial^2}{\partial Y^2}+\varepsilon_{33}\frac{\partial^2}{\partial Z^2})\phi-(g_{11}\frac{\partial^2}{\partial X^2}+g_{11}\frac{\partial^2}{\partial Y^2}+g_{33}\frac{\partial^2}{\partial Z^2})\varphi=0,\end{aligned} \tag{16}$$

$$\begin{aligned}&(d_{15}+d_{31})(\frac{\partial^2 u_x}{\partial X\partial Z}+\frac{\partial^2 u_y}{\partial Y\partial Z})+(d_{15}\frac{\partial^2}{\partial X^2}+d_{15}\frac{\partial^2}{\partial Y^2}+d_{33}\frac{\partial^2}{\partial Z^2})u_z-(g_{11}\frac{\partial^2}{\partial X^2}\\&+g_{11}\frac{\partial^2}{\partial Y^2}+g_{33}\frac{\partial^2}{\partial Z^2})\phi-(\mu_{11}\frac{\partial^2}{\partial X^2}+\mu_{11}\frac{\partial^2}{\partial Y^2}+\mu_{33}\frac{\partial^2}{\partial Z^2})\varphi=0,\end{aligned} \tag{17}$$

2.3 General solutions

Following the way in (Chen et al., 2004; Hu, 1953), two displacement functions, H and G, are introduced to express displacements u_x and u_y, namely,

$$u_x=\frac{\partial H}{\partial Y}-\frac{\partial G}{\partial X},\ u_y=-\frac{\partial H}{\partial X}-\frac{\partial G}{\partial Y}. \tag{18}$$

Substituting Eq. (18) into Eqs. (13-17) results in the governing equations in terms of the displacement functions, H and G,

$$[c_{66}\Lambda + c_{44}(1-c^2)\frac{\partial^2}{\partial Z^2}]H = 0, \tag{19}$$

$$[D][G \quad u_z \quad \phi \quad \varphi]^T = 0, \tag{20}$$

where $[D]$ is a differential operator matrix given by,

$$[D] = \begin{bmatrix} c_{11}\Lambda + c_{44}(1-c^2)\frac{\partial^2}{\partial Z^2} & -(c_{13}+c_{44})\frac{\partial}{\partial Z} & -(e_{15}+e_{31})\frac{\partial}{\partial Z} & -(d_{15}+d_{31})\frac{\partial}{\partial Z} \\ -(c_{13}+c_{44})\Lambda\frac{\partial}{\partial Z} & c_{44}\Lambda + (c_{33}-c_{44}c^2)\frac{\partial^2}{\partial Z^2} & e_{15}\Lambda + e_{33}\frac{\partial^2}{\partial Z^2} & d_{15}\Lambda + d_{33}\frac{\partial^2}{\partial Z^2} \\ (e_{15}+e_{31})\Lambda\frac{\partial}{\partial Z} & -(e_{15}\Lambda + e_{33}\frac{\partial^2}{\partial Z^2}) & \varepsilon_{11}\Lambda + \varepsilon_{33}\frac{\partial^2}{\partial Z^2} & g_{11}\Lambda + g_{33}\frac{\partial^2}{\partial Z^2} \\ (d_{15}+d_{31})\Lambda\frac{\partial}{\partial Z} & -(d_{15}\Lambda + d_{33}\frac{\partial^2}{\partial Z^2}) & g_{11}\Lambda + g_{33}\frac{\partial^2}{\partial Z^2} & \mu_{11}\Lambda + \mu_{33}\frac{\partial^2}{\partial Z^2} \end{bmatrix}, \tag{21}$$

with $\Lambda = \frac{\partial^2}{\partial X^2} + \frac{\partial^2}{\partial Y^2}$.

Another new displacement function, F, is introduced; it satisfies the relation of $|D|F = 0$. The determinant of matrix $[D]$ can be calculated, which leads to the following,

$$(n_0\frac{\partial^8}{\partial Z^8} + n_1\Lambda\frac{\partial^6}{\partial Z^6} + n_2\Lambda^2\frac{\partial^4}{\partial Z^4} + n_3\Lambda^3\frac{\partial^2}{\partial Z^2} + n_4\Lambda^4)F = 0 \tag{22}$$

where $n_0, n_1, ..., n_4$ are given in Appendix A.

Therefore, displacement function G, displacement u_z, electric potential ϕ and magnetic potential φ in Eq. (20) can be rewritten in terms of function F,

$$G = A_{i1}F,\ u_z = A_{i2}F,\ \phi = A_{i3}F,\ \varphi = A_{i4}F, (i = 1,2,3,4). \tag{23}$$

where A_{ij} are the cofactors of matrix $[D]$. Substituting Eq. (23) into Eq. (18) results in the following,

$$u_x = \frac{\partial H}{\partial Y} - A_{i1}\frac{\partial F}{\partial X},\ u_y = -\frac{\partial H}{\partial X} - A_{i1}\frac{\partial F}{\partial Y}. \tag{24}$$

Furthermore, substituting Eqs. (23) and (24) into Eq. (2) and then substituting the results into Eq. (1), the stresses, electric displacements and magnetic inductions can be expressed in terms of displacement functions H and F.

On the other hand, Eq. (22) can be simplified with the assistance of the Vieta theorem for the property of roots, the results are

$$(\Lambda+\frac{\partial^2}{\partial Z_1^2})(\Lambda+\frac{\partial^2}{\partial Z_2^2})(\Lambda+\frac{\partial^2}{\partial Z_3^2})(\Lambda+\frac{\partial^2}{\partial Z_4^2})F=0, \tag{25}$$

where $Z_i^2 = s_i^2 Z^2, (i = 1, 2, 3, \text{and } 4)$, and s_i are deterimined by four of the roots of the following equation, whose real portions are positive:

$$n_0 s^8 - n_1 s^6 + n_2 s^4 - n_3 s^2 + n_4 = 0. \tag{26}$$

Turning attention to Eq. (19), it can be rewritten as

$$[\Lambda+\frac{\partial^2}{\partial Z_0^2}]H=0, \tag{27}$$

where $Z_0^2 = s_0^2 Z^2$ with $s_0^2 = c_{66}/[c_{44}(1-c^2)]$.

By utilizing the generalized Almansi's theorem (Ding, 1996), the displacement function F in Eq. (25) can be expressed in terms of four quasi-harmonic functions, given as follows,

$$\begin{aligned}
&\text{Case 1:}\ F = F_1 + F_2 + F_3 + F_4,\ s_1 \neq s_2 \neq s_3 \neq s_4,;\\
&\text{Case 2:}\ F = F_1 + F_2 + F_3 + ZF_4,\ s_1 \neq s_2 \neq s_3 = s_4;\\
&\text{Case 3:}\ F = F_1 + F_2 + ZF_3 + Z^2F_4,\ s_1 \neq s_2 = s_3 = s_4;\\
&\text{Case 4:}\ F = F_1 + ZF_2 + Z_2F_3 + Z^3F_4,\ s_1 = s_2 = s_3 = s_4,
\end{aligned} \tag{28}$$

where Eq. (25) can be rewritten as

$$(\Lambda+\frac{\partial^2}{\partial Z_i^2})F_i=0, (i=1,2,3,4). \tag{29}$$

Considering a large amount of MEE materials belonging to Case 1 of Eq. (28) (Chen et al., 2010; Li et al., 2015b; Li et al., 2014; Pan, 2001), the present work is only confined to study Case 1, which is with distinct s_i. As suggested by Ding et al. (Ding, 1996), five harmonic functions ψ_i, which can be expressed as $\alpha_i s_i \partial^3 F_i/\partial Z_i^3 = \psi_i$ $(i = 1,2,3,4, \text{and}$ H is written as $\psi_0)$, are introduced to further simplify the expressions (23, 24). Thus the general solutions in the case of distinct s_i can be expressed in terms of ψ_i as,

$$\begin{aligned}
&U=\nabla\left(\sum_{j=1}^{4}\psi_j+\mathrm{i}\psi_0\right),\quad w_m=\sum_{j=1}^{4}s_j k_{mj}\psi_{j,Z_j},\\
&\sigma_1=2\sum_{j=1}^{4}\left(c_{66}-s_j^2\omega_{1j}\right)\psi_{j,Z_jZ_j},\quad \sigma_2=2c_{66}\nabla^2\left(\sum_{j=1}^{4}\psi_j+\mathrm{i}\psi_0\right),\\
&\sigma_{zm}=\sum_{j=1}^{4}\omega_{mj}\psi_{j,Z_jZ_j},\quad \tau_{zm}=\nabla\left(\sum_{j=1}^{4}s_j\omega_{mj}\psi_{j,Z_j}+\mathrm{i}s_0\rho_m\psi_{0,Z_0}\right),\quad (m=1,2,3),
\end{aligned} \tag{30}$$

where

$$
\begin{aligned}
&U = u_x + \mathrm{i}u_y,\ w_1 = u_z,\ \ w_2 = \phi,\ \ w_3 = \varphi,\\
&\sigma_1 = \sigma_{xx} + \sigma_{yy},\ \ \sigma_2 = \sigma_{xx} - \sigma_{yy} + 2\mathrm{i}\sigma_{xy},\\
&\sigma_{z1} = \sigma_{zz},\ \ \sigma_{z2} = D_z,\ \ \sigma_{z3} = B_z,\\
&\tau_{z1} = \sigma_{xz} + \mathrm{i}\sigma_{yz},\ \ \tau_{z2} = D_x + \mathrm{i}D_y,\ \ \tau_{z3} = B_x + \mathrm{i}B_y.
\end{aligned}
\tag{31}
$$

Note that the Einstein summation convention is not used for repeated index here; and $\nabla = \partial/\partial X + \mathrm{i}\partial/\partial Y$. Harmonic functions ψ_i satisfy the quasi-Laplace equation as follows,

$$
(\Lambda + \frac{\partial^2}{\partial Z_i^2})\psi_i = 0,\ (i = 0,1,\ldots,4). \tag{32}
$$

2.4 Frequency response functions and Influence coefficients

Because Ψ_i in Eq. (32) are harmonic functions, double Fourier transforms of these functions can be expressed in terms of exponential functions with unknown coefficients, as suggested in (Wang et al., 2015; Yu et al., 2014). Hence, the following direct double Fourier transform and its inverse are introduced,

$$
\begin{aligned}
&\tilde{\tilde{f}}(m,n,Z) = \int_{-\infty}^{\infty}\int_{-\infty}^{\infty} f(X,Y,Z)e^{-\mathrm{i}(mX+nY)}dXdY,\\
&f(X,Y,Z) = \frac{1}{4\pi^2}\int_{-\infty}^{\infty}\int_{-\infty}^{\infty} \tilde{\tilde{f}}(m,n,Z)e^{\mathrm{i}(mX+nY)}dmdn,
\end{aligned}
\tag{33}
$$

where hat "≈" denotes the double Fourier transform; m and n represent the transform variables with respect to the X and Y directions, respectively, but in the frequency domain.

Applying Fourier transforms to Eq. (32) results in the following,

$$
\tilde{\tilde{\psi}}_i = A_i(m,n)e^{-\alpha Z_i} + \bar{A}_i(m,n)e^{\alpha Z_i}\quad (i = 0,\ldots 4), \tag{34}
$$

where $\alpha = \sqrt{m^2 + n^2}$; $A_i(m,n)$ and $\bar{A}_i(m,n)$ are ten unknowns to be determined from the boundary conditions.

Applying Fourier transforms to Eq. (30) and substituting Eq. (34) into the results lead to the transformed displacements, electric potentials, magnetic potentials, stresses, electric displacements, and magnetic inductions, expressed as

$$
\begin{aligned}
\tilde{\tilde{u}}_x &= -\mathrm{i}nA_0 e^{-\alpha s_0 Z} - \mathrm{i}n\bar{A}_0 e^{\alpha s_0 Z} + \sum_{j=1}^{4} \mathrm{i}mA_j e^{-\alpha s_j Z} + \sum_{j=1}^{4} \mathrm{i}m\bar{A}_j e^{\alpha s_j Z}, \\
\tilde{\tilde{u}}_y &= \mathrm{i}mA_0 e^{-\alpha s_0 Z} + \mathrm{i}m\bar{A}_0 e^{\alpha s_0 Z} + \sum_{j=1}^{4} \mathrm{i}nA_j e^{-\alpha s_j Z} + \sum_{j=1}^{4} \mathrm{i}n\bar{A}_j e^{\alpha s_j Z}, \\
\tilde{\tilde{u}}_z &= -\sum_{j=1}^{4} s_j k_{1j} \alpha A_j e^{-\alpha s_j Z} + \sum_{j=1}^{4} s_j k_{1j} \alpha \bar{A}_j e^{\alpha s_j Z}, \\
\tilde{\tilde{\phi}} &= -\sum_{j=1}^{4} s_j k_{2j} \alpha A_j e^{-\alpha s_j Z} + \sum_{j=1}^{4} s_j k_{2j} \alpha \bar{A}_j e^{\alpha s_j Z}, \\
\tilde{\tilde{\varphi}} &= -\sum_{j=1}^{4} s_j k_{3j} \alpha A_j e^{-\alpha s_j Z} + \sum_{j=1}^{4} s_j k_{3j} \alpha \bar{A}_j e^{\alpha s_j Z},
\end{aligned}
\tag{35}
$$

$$
\begin{aligned}
\tilde{\tilde{\sigma}}_{xx} &= 2c_{66} mnA_0 e^{-\alpha s_0 Z} + \sum_{j=1}^{4} [(c_{66} s_j^2 \omega_{1j} \alpha^2) + c_{66}(\tfrac{2}{6} m^2 A_j) e^{-\alpha s_j Z} \\
&\quad + 2c_{66} mn\bar{A}_0 e^{\alpha s_0 Z} + \sum_{j=1}^{4} [(c_{66} s_j^2 \omega_{1j} \alpha^2) + c_{66}(\tfrac{2}{6} m^2 \bar{A}_j) e^{\alpha s_j Z} \\
\tilde{\tilde{\sigma}}_{yy} &= -2c_{66} mnA_0 e^{-\alpha s_0 Z} + \sum_{j=1}^{4} [(c_{66} s_j^2 \omega_{1j} \alpha^2) - c_{66}(\tfrac{2}{6} m^2 A_j) e^{-\alpha s_j Z} \\
&\quad - 2c_{66} mn\bar{A}_0 e^{\alpha s_0 Z} + \sum_{j=1}^{4} [(c_{66} s_j^2 \omega_{1j}) \alpha^2 - c_{66}(n^2 - m^2)] \bar{A}_j e^{\alpha s_j Z}, \\
\tilde{\tilde{\sigma}}_{zz} &= \sum_{j=1}^{4} \omega_{1j} \alpha^2 A_j e^{-\alpha s_j Z} + \sum_{j=1}^{4} \omega_{1j} \alpha^2 \bar{A}_j e^{\alpha s_j Z}, \\
\tilde{\tilde{\sigma}}_{xy} &= c_{66}(n^2 - m^2) A_0 e^{-\alpha s_0 Z} - \sum_{j=1}^{4} 2c_{66} mnA_j e^{-\alpha s_j Z} \\
&\quad + c_{66}(n^2 - m^2) \bar{A}_0 e^{\alpha s_0 Z} - \sum_{j=1}^{4} 2c_{66} mn\bar{A}_j e^{\alpha s_j Z}, \\
\tilde{\tilde{\sigma}}_{xz} &= \mathrm{i}ns_0 \rho_1 \alpha A_0 e^{-\alpha s_0 Z} - \sum_{j=1}^{4} \mathrm{i}ms_j \omega_{1j} \alpha A_j e^{-\alpha s_j Z} \\
&\quad - \mathrm{i}ns_0 \rho_1 \alpha \bar{A}_0 e^{\alpha s_0 Z} + \sum_{j=1}^{4} \mathrm{i}ms_j \omega_{1j} \alpha \bar{A}_j e^{\alpha s_j Z}, \\
\tilde{\tilde{\sigma}}_{yz} &= -\mathrm{i}ms_0 \rho_1 \alpha A_0 e^{-\alpha s_0 Z} - \sum_{j=1}^{4} \mathrm{i}ns_j \omega_{1j} \alpha A_j e^{-\alpha s_j Z} \\
&\quad + \mathrm{i}ms_0 \rho_1 \alpha \bar{A}_0 e^{\alpha s_0 Z} + \sum_{j=1}^{4} \mathrm{i}ns_j \omega_{1j} \alpha \bar{A}_j e^{\alpha s_j Z},
\end{aligned}
\tag{36}
$$

ACCEPTED MANUSCRIPT

$$\tilde{\tilde{D}}_x = \mathrm{i}ns_0\rho_2\alpha A_0 e^{-\alpha s_0 Z} - \sum_{j=1}^{4}\mathrm{i}ms_j\omega_{2j}\alpha A_j e^{-\alpha s_j Z}$$
$$-\mathrm{i}ns_0\rho_2\alpha \bar{A}_0 e^{\alpha s_0 Z} + \sum_{j=1}^{4}\mathrm{i}ms_j\omega_{2j}\alpha \bar{A}_j e^{\alpha s_j Z},$$
$$\tilde{\tilde{D}}_y = -\mathrm{i}ms_0\rho_2\alpha A_0 e^{-\alpha s_0 Z} - \sum_{j=1}^{4}\mathrm{i}ns_j\omega_{2j}\alpha A_j e^{-\alpha s_j Z} \tag{37}$$
$$+\mathrm{i}ms_0\rho_2\alpha \bar{A}_0 e^{\alpha s_0 Z} + \sum_{j=1}^{4}\mathrm{i}ns_j\omega_{2j}\alpha \bar{A}_j e^{\alpha s_j Z},$$
$$\tilde{\tilde{D}}_z = \sum_{j=1}^{4}\omega_{2j}\alpha^2 A_j e^{-\alpha s_j Z} + \sum_{j=1}^{4}\omega_{2j}\alpha^2 \bar{A}_j e^{\alpha s_j Z},$$
$$\tilde{\tilde{B}}_x = \mathrm{i}ns_0\rho_3\alpha A_0 e^{-\alpha s_0 Z} - \sum_{j=1}^{4}\mathrm{i}ms_j\omega_{3j}\alpha A_j e^{-\alpha s_j Z}$$
$$-\mathrm{i}ns_0\rho_3\alpha \bar{A}_0 e^{\alpha s_0 Z} + \sum_{j=1}^{4}\mathrm{i}ms_j\omega_{3j}\alpha \bar{A}_j e^{\alpha s_j Z},$$
$$\tilde{\tilde{B}}_y = -\mathrm{i}ms_0\rho_3\alpha A_0 e^{-\alpha s_0 Z} - \sum_{j=1}^{4}\mathrm{i}ns_j\omega_{3j}\alpha A_j e^{-\alpha s_j Z} \tag{38}$$
$$+\mathrm{i}ms_0\rho_3\alpha \bar{A}_0 e^{\alpha s_0 Z} + \sum_{j=1}^{4}\mathrm{i}ns_j\omega_{3j}\alpha \bar{A}_j e^{\alpha s_j Z},$$
$$\tilde{\tilde{B}}_z = \sum_{j=1}^{4}\omega_{3j}\alpha^2 A_j e^{-\alpha s_j Z} + \sum_{j=1}^{4}\omega_{3j}\alpha^2 \bar{A}_j e^{\alpha s_j Z}.$$

Then applying the Fourier transform to Eqs. (4, 5) and substituting Eqs. (35-38) into the results lead to a series of boundary conditions in the Fourier transform domain,

$$ns_0\rho_1 A_0 - ns_0\rho_1\bar{A}_0 - m\sum_{j=1}^{4}s_j\omega_{1j}A_j + m\sum_{j=1}^{4}s_j\omega_{1j}\bar{A}_j = 0, \tag{39}$$

$$-ms_0\rho_1 A_0 + ms_0\rho_1\bar{A}_0 - n\sum_{j=1}^{4}s_j\omega_{1j}A_j + n\sum_{j=1}^{4}s_j\omega_{1j}\bar{A}_j = 0, \tag{40}$$

$$\sum_{j=1}^{4}\omega_{1j}A_j + \sum_{j=1}^{4}\omega_{1j}\bar{A}_j = -\tilde{\tilde{p}}/\alpha^2, \tag{41}$$

$$\sum_{j=1}^{4}\omega_{2j}A_j + \sum_{j=1}^{4}\omega_{2j}\bar{A}_j = -q/\alpha^2, \tag{42}$$

$$\sum_{j=1}^{4}\omega_{3j}A_j + \sum_{j=1}^{4}\omega_{3j}\bar{A}_j = -g/\alpha^2, \tag{43}$$

$$ne^{-\alpha s_0 h_t} A_0 + ne^{\alpha s_0 h_t} \bar{A}_0 - \sum_{j=1}^{4} me^{-\alpha s_j h_t} A_j - \sum_{j=1}^{4} me^{\alpha s_j h_t} \bar{A}_j = 0, \tag{44}$$

$$me^{-\alpha s_0 h_t} A_0 + me^{\alpha s_0 h_t} \bar{A}_0 + \sum_{j=1}^{4} ne^{-\alpha s_j h_t} A_j + \sum_{j=1}^{4} ne^{\alpha s_j h_t} \bar{A}_j = 0, \tag{45}$$

$$\sum_{j=1}^{4} s_j k_{1j} e^{-\alpha s_j h_t} A_j - \sum_{j=1}^{4} s_j k_{1j} e^{\alpha s_j h_t} \bar{A}_j = 0, \tag{46}$$

$$\sum_{j=1}^{4} s_j k_{2j} e^{-\alpha s_j h_t} A_j - \sum_{j=1}^{4} s_j k_{2j} e^{\alpha s_j h_t} \bar{A}_j = 0, \tag{47}$$

$$\sum_{j=1}^{4} s_j k_{3j} e^{-\alpha s_j h_t} A_j - \sum_{j=1}^{4} s_j k_{3j} e^{\alpha s_j h_t} \bar{A}_j = 0. \tag{48}$$

Solving the above equation set results in the following,

$$\begin{aligned}
A_1 &= [q^{(1)} h_2^{(2)} - q^{(2)} h_2^{(1)}] / [h_1^{(1)} h_2^{(2)} - h_2^{(1)} h_1^{(2)}], \\
A_2 &= [q^{(2)} - h_1^{(2)} A_1] / h_2^{(2)}, \\
A_3 &= [p^{(3)} - \sum_{j=1}^{2} l_j^{(3)} A_j] / l_3^{(3)}, \\
A_4 &= [-\sum_{j=1}^{3} k_j^{(4)} A_j] / k_4^{(4)}, \\
\bar{A}_1 &= -\sum_{j=1}^{4} s_j^{(5)} A_j / \bar{s}_1^{(5)}, \\
\bar{A}_2 &= [-\sum_{j=1}^{4} t_{2j}^{(1)} e^{-\alpha(s_j+s_2)} A_j - \bar{t}_{21}^{(1)} e^{\alpha(s_1-s_2)h_t} \bar{A}_1] / \bar{t}_{22}^{(1)}, \\
\bar{A}_3 &= [-\sum_{j=1}^{4} k_j e^{-\alpha(s_j+s_3)h_t} A_j - \sum_{j=1}^{2} \bar{k}_j e^{\alpha(s_j-s_3)h_t} \bar{A}_j] / \bar{k}_3, \\
\bar{A}_4 &= -\sum_{j=1}^{4} e^{-\alpha(s_j+s_4)h_t} A_j - \sum_{j=1}^{3} e^{\alpha(s_j-s_4)h_t} \bar{A}_j, \\
A_0 &= -\sum_{j=1}^{4} n(r_j A_j - \bar{r}_j \bar{A}_j) / (mr_0), \\
\bar{A}_0 &= [-\sum_{j=1}^{4} n(e^{-\alpha(s_j+s_4)h_t} A_j - e^{\alpha(s_j-s_4)h_t} \bar{A}_j) - me^{-\alpha(s_0+s_4)h_t} A_0] / (me^{\alpha(s_0-s_4)h_t}).
\end{aligned} \tag{49}$$

The constants, p, q, h, l, k, t and r, in Eq. (49) are listed in Appendix B.

Accordingly, substituting coefficients $\{A_0, \dots, A_4, \bar{A}_0, \dots, \bar{A}_4\}$ back into Eqs. (35-38) establishes the Fourier transformed solutions for the corresponding elastic displacements,

ACCEPTED MANUSCRIPT

electric/magnetic potentials, stresses, electric displacements, and magnetic inductions.

The frequency response functions (FRFs) are related to material properties and a certain velocity, V, can be described as the responses to unit point loads. The components of the FRFs can be analytically obtained by letting $\tilde{\tilde{p}} = 1$, $\tilde{\tilde{q}} = 1$ or $\tilde{\tilde{g}} = 1$ in Eq. (35-38), which are denoted by

$$\begin{bmatrix} \tilde{\tilde{G}}^{u_i} \\ \tilde{\tilde{G}}^{\phi} \\ \tilde{\tilde{G}}^{\varphi} \\ \tilde{\tilde{G}}^{\sigma_{ij}} \\ \tilde{\tilde{G}}^{D_i} \\ \tilde{\tilde{G}}^{B_i} \end{bmatrix} = \begin{bmatrix} \tilde{\tilde{G}}^{u_i}_{\tilde{\tilde{p}}=1} & \tilde{\tilde{G}}^{u_i}_{\tilde{\tilde{q}}=1} & \tilde{\tilde{G}}^{u_i}_{\tilde{\tilde{g}}=1} \\ \tilde{\tilde{G}}^{\phi}_{\tilde{\tilde{p}}=1} & \tilde{\tilde{G}}^{\phi}_{\tilde{\tilde{q}}=1} & \tilde{\tilde{G}}^{\phi}_{\tilde{\tilde{g}}=1} \\ \tilde{\tilde{G}}^{\varphi}_{\tilde{\tilde{p}}=1} & \tilde{\tilde{G}}^{\varphi}_{\tilde{\tilde{q}}=1} & \tilde{\tilde{G}}^{\varphi}_{\tilde{\tilde{g}}=1} \\ \tilde{\tilde{G}}^{\sigma_{ij}}_{\tilde{\tilde{p}}=1} & \tilde{\tilde{G}}^{\sigma_{ij}}_{\tilde{\tilde{q}}=1} & \tilde{\tilde{G}}^{\sigma_{ij}}_{\tilde{\tilde{g}}=1} \\ \tilde{\tilde{G}}^{D_i}_{\tilde{\tilde{p}}=1} & \tilde{\tilde{G}}^{D_i}_{\tilde{\tilde{q}}=1} & \tilde{\tilde{G}}^{D_i}_{\tilde{\tilde{g}}=1} \\ \tilde{\tilde{G}}^{B_i}_{\tilde{\tilde{p}}=1} & \tilde{\tilde{G}}^{B_i}_{\tilde{\tilde{q}}=1} & \tilde{\tilde{G}}^{B_i}_{\tilde{\tilde{g}}=1} \end{bmatrix}, \tag{50}$$

where $\tilde{\tilde{G}}^{u}_{p}$ denotes the FRFs of u excited by load p, and $\tilde{\tilde{G}}^{\varphi}_{p}$ represents the FRFs of magnetic potential φ caused by pressure p and so on.

Once the FRFs are obtained, the continuous Fourier transforms of influence coefficients (ICs) can be solved by multiplying the FRFs and the Fourier transformed shape functions (Liu and Wang, 2002),

$$\begin{bmatrix} \tilde{\tilde{C}}^{u_i} & \tilde{\tilde{C}}^{\phi} & \tilde{\tilde{C}}^{\varphi} & \tilde{\tilde{C}}^{\sigma_{ij}} & \tilde{\tilde{C}}^{D_i} & \tilde{\tilde{C}}^{B_i} \end{bmatrix}^T = \begin{bmatrix} \tilde{\tilde{G}}^{u_i} & \tilde{\tilde{G}}^{\phi} & \tilde{\tilde{G}}^{\varphi} & \tilde{\tilde{G}}^{\sigma_{ij}} & \tilde{\tilde{G}}^{D_i} & \tilde{\tilde{G}}^{B_i} \end{bmatrix}^T \cdot \tilde{\tilde{F}}_s, \tag{51}$$

where F_s is the shape function given as follows

$$F_s(X,Y) = \begin{cases} 1, & |X| \le \Delta_X/2 \text{ and } |Y| \le \Delta_Y/2, \\ 0, & \text{others}, \end{cases} \quad \text{and} \tag{52}$$
$$\tilde{\tilde{F}}_s(m,n) = \frac{4\sin(m\Delta_X/2)\sin(n\Delta_Y/2)}{mn}.$$

Then the discrete Fourier transforms of ICs can be further calculated from the continuous ICs with the following aliasing treatments (Liu and Wang, 2002; Wang et al., 2015),

$$\hat{\tilde{C}} = \frac{1}{\Delta_X \Delta_Y} \sum_{r_X=-AL}^{r_X=AL} \sum_{r_Y=-AL}^{r_Y=AL} \tilde{\tilde{C}}\left(\frac{2\pi}{M_e \Delta_X} i - \frac{2\pi}{\Delta_X} r_X, \frac{2\pi}{N_e \Delta_Y} j - \frac{2\pi}{\Delta_Y} r_Y\right), \tag{53}$$
$$(-M_e/2 < i \le M_e/2, -N_e/2 < j \le N_e/2),$$

where Δ_X and Δ_Y are the mesh sizes along the X and Y directions, respectively; AL represents the level of the aliasing control; $M_e = 2^{\gamma} M$ and $N_e = 2^{\gamma} N$ denote the refinement mesh numbers of the original mesh numbers M and N; C is the ICs in the form of the discrete

Fourier transform.

Furthermore, the displacement, stress, electric/magnetic potential, electric displacement, and magnetic induction can be obtained by utilizing the same discrete convolution-fast Fourier transform (DC-FFT) algorithm for pressure, surface electric charge, and surface magnetic charge by means of the corresponding components of ICs (Liu et al., 2007; Liu and Wang, 2002) with *IFFT* being the inverse fast Fourier transform:

$$u_i = IFFT(\hat{\hat{C}}^{u_i} \cdot [\hat{\hat{p}} \;\; \hat{\hat{q}} \;\; \hat{\hat{g}}]^T) = IFFT(\hat{\hat{C}}^{u_i}_{\tilde{p}=1}\hat{\hat{p}} + \hat{\hat{C}}^{u_i}_{\tilde{q}=1}\hat{\hat{q}} + \hat{\hat{C}}^{u_i}_{\tilde{g}=1}\hat{\hat{g}}), \tag{54}$$

$$\phi = IFFT(\hat{\hat{C}}^{\phi} \cdot [\hat{\hat{p}} \;\; \hat{\hat{q}} \;\; \hat{\hat{g}}]^T) = IFFT(\hat{\hat{C}}^{\phi}_{\tilde{p}=1}\hat{\hat{p}} + \hat{\hat{C}}^{\phi}_{\tilde{q}=1}\hat{\hat{q}} + \hat{\hat{C}}^{\phi}_{\tilde{g}=1}\hat{\hat{g}}), \tag{55}$$

$$\varphi = IFFT(\hat{\hat{C}}^{\varphi} \cdot [\hat{\hat{p}} \;\; \hat{\hat{q}} \;\; \hat{\hat{g}}]^T) = IFFT(\hat{\hat{C}}^{\varphi}_{\tilde{p}=1}\hat{\hat{p}} + \hat{\hat{C}}^{\varphi}_{\tilde{q}=1}\hat{\hat{q}} + \hat{\hat{C}}^{\varphi}_{\tilde{g}=1}\hat{\hat{g}}), \tag{56}$$

$$\sigma_{ij} = IFFT(\hat{\hat{C}}^{\sigma_{ij}} \cdot [\hat{\hat{p}} \;\; \hat{\hat{q}} \;\; \hat{\hat{g}}]^T) = IFFT(\hat{\hat{C}}^{\sigma_{ij}}_{\tilde{p}=1}\hat{\hat{p}} + \hat{\hat{C}}^{\sigma_{ij}}_{\tilde{q}=1}\hat{\hat{q}} + \hat{\hat{C}}^{\sigma_{ij}}_{\tilde{g}=1}\hat{\hat{g}}), \tag{57}$$

$$D_i = IFFT(\hat{\hat{C}}^{D_i} \cdot [\hat{\hat{p}} \;\; \hat{\hat{q}} \;\; \hat{\hat{g}}]^T) = IFFT(\hat{\hat{C}}^{D_i}_{\tilde{p}=1}\hat{\hat{p}} + \hat{\hat{C}}^{D_i}_{\tilde{q}=1}\hat{\hat{q}} + \hat{\hat{C}}^{D_i}_{\tilde{g}=1}\hat{\hat{g}}), \tag{58}$$

$$B_i = IFFT(\hat{\hat{C}}^{B_i} \cdot [\hat{\hat{p}} \;\; \hat{\hat{q}} \;\; \hat{\hat{g}}]^T) = IFFT(\hat{\hat{C}}^{B_i}_{\tilde{p}=1}\hat{\hat{p}} + \hat{\hat{C}}^{B_i}_{\tilde{q}=1}\hat{\hat{q}} + \hat{\hat{C}}^{B_i}_{\tilde{g}=1}\hat{\hat{g}}). \tag{59}$$

2.5 Numerical modeling

Now the working progress of the MEE energy converter system shown in Fig. 1(a), under an varying applied force *P*(*t*) along the *z* axis can be solved. The loading velocity of the rigid sphere is assumed to be a function of loading time *t*, which can be expresses as either

$$V = \begin{cases} 2V_0 \cdot t / T_{total}, & \text{for } 0 \le t < T_{total}/2, \\ 2V_0 \cdot (1 - t / T_{total}), & \text{for } T_{total}/2 \le t < T_{total}, \end{cases} \tag{60}$$

or

$$V = V_0 \sin(\pi t / T_{total}), \tag{61}$$

for the triangular and sinusoidal variations, respectively, where V_0 denotes the maximum value of the loading velocity; T_{total} represents the total time during one loading cycle.

The working progress of the MEE system depends on the loading history, for which the dynamic contact problem is solved first. For a certain time *t*, the following contact conditions for displacement, pressure, and load are applicable to such a dynamic contact problem,

$$\bar{u}_z^t = g_z^t - h_0^t, \tag{62}$$

$$\begin{aligned} p^t > 0 \,\&\, g_z^t = 0 \Rightarrow \forall (x, y) \in \Gamma_c, \\ p^t = 0 \,\&\, g_z^t > 0 \Rightarrow \forall (x, y) \notin \Gamma_c, \end{aligned} \tag{63}$$

$$\int_{\Gamma_c} p^t dxdy = P^t + M_s a^t, \tag{64}$$

where $\bar{u}_z^t$ is the surface normal displacement for the MEE film; g_z^t is the gap between the surfaces of the rigid sphere and the MEE film; Γ_c is the contact zone; h_0^t is the initial vertical separation; M_s is the mass of the sphere; a^t is the acceleration of the rigid sphere at time t; and P^t represents the applied force at time t. For the velocity type given by Eq (60), a^t equals $2V_0/T_{total}$ for $0<t<T_{total}/2$ and equals $-2V_0/T_{total}$ for $T_{total}/2<t<T_{total}$. For the velocity type given by Eq. (61), $a^t = \{\sin[2\pi(t+\Delta t)/T_{total}] - \sin(2\pi t/T_{total})\}/\Delta t$. It should be mentioned that the applied force P^t gradually increases with indentation depth. Thus for a given indentation depth δ^t at time t, P^t should be determined in an iteration process, as described below.

In the numerical process, the DC-FFT algorithm described in (Liu et al., 2007; Zhang et al., 2018) is applied to solve Eqs. (54-59) in order to obtain the displacement component u_i, electric potential ϕ, magnetic potential φ, elastic stress tensor σ_{ij}, electric displacement vector D_i, and magnetic induction vector B_i. Once the surface displacement $\bar{u}_z^t$ is obtained, gap g^t in Eq. (62) can be solved. Pressure p^t in Eq. (63) is calculated with the conjugate gradient method (CGM) described in (Polonsky and Keer, 1999). Figure 2 shows the flow diagram for the numerical approach, in which,

(1) Initial parameters are input, including material properties, mesh size and geometry information, etc. The initial surface electric/magnetic charges, applied force, loading time are set to zero.

(2) The loading time, t, is increased step by step. In each increment step Δt, the accumulated time is updated.

(3) At time t, the velocity of the rigid sphere is calculated based on Eqs. (60, 61). Moreover, the ICs should be prepared in advance based on the material properties and the current velocity.

(4) The accumulated indentation depth is calculated based on $\delta^t = \delta^{t-1} + V(t)\cdot\Delta t$.

(5) In current indentation depth, δ^t, the total force, P^t, is applied step by step. In each increment step ΔP, pressure p^t is calculated using the CGM.

The CGM implementation and the iteration procedure involve: 1) estimation of pressure distribution p^t; 2) calculation of surface normal displacement $\bar{u}_z^t$ in Eq. (54) by means of the DC-FFT algorithm; 3) acquisition of gap g_z^t by Eq. (62); 4) updates of pressure p^t in step t based on the descent direction, d_{cgm}, and the step length, a_{cgm}; 5) implementation of Eq. (64) to confirm that the applied force has been enforced; and 6) convergence tests in the iteration steps, 2-5, until the required convergence condition is satisfied.

(6) Once the new value of p^t is obtained, the surface normal displacement, u_{z0}, at the contact center, namely the calculated indentation depth, can be solved by Eq. (54).

(7) Iteration steps (5, 6) are continued until the calculated u_{z0} at time t approaches δ^t. At

this point, the applied force P^t at time t for the current indentation depth δ^t is obtained. Moreover, the current pressure distribution p^t can be solved.

(8) The accumulated surface electric charge q^t and magnetic charge g^t, which equal the normal electric displacement D_z and magnetic induction B_z at the contact surface, respectively, can be solved based on pressure p^t, surface electric charge q^{t-1}, and surface magnetic charge g^{t-1} by Eqs. (58, 59). Furthermore, loading velocity V, applied force P, pressure p, surface electric charge q, surface magnetic charge g, surface electric potential ϕ, and surface magnetic potential φ are recorded at time t.

(9) Iteration steps (2)-(8) are continued until the total loading time, T_{total}, is reached. At this point, the working progress of the MEE energy conversion during one loading cycle is completed, in which the electric potential generated at the top surface of the MEE film should drive the electron flow through the circuit.

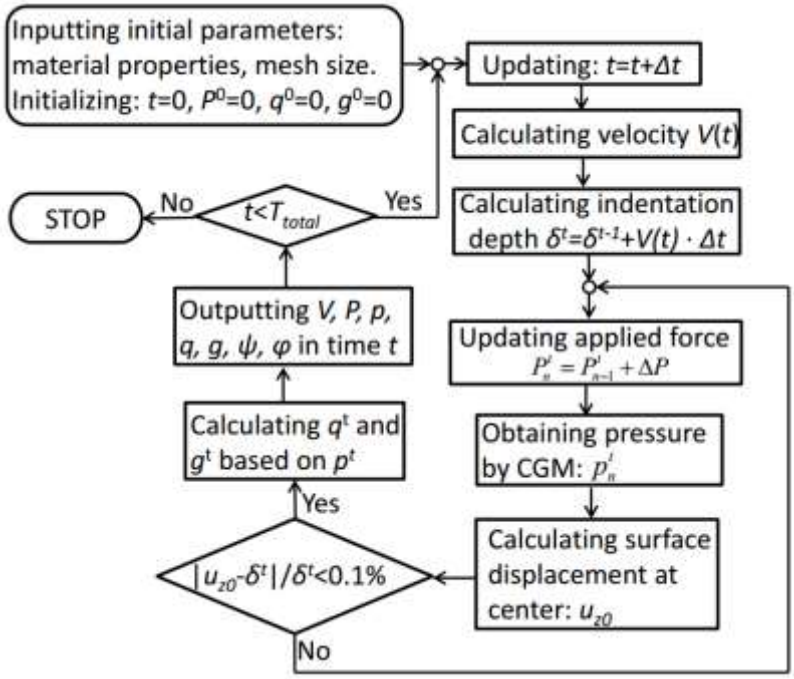

Fig. 2. Flow diagram for modeling the working progress of the MEE energy conversion.

3. Results and discussion

The working progress of the MEE conversion of the dynamic contact energy the rigid sphere on the top surface of the transversely isotropic multiferroic MEE film, described as the system in Fig. 1(a) under an increasing applied force $P(t)$ along the z axis, was solved based on the efficient SAM approach derived in the previous section. A fixed computational domain of $4a_0 \times 4a_0 \times h_t$ with $256 \times 256 \times 64$ grids in the X, Y and Z directions was used, where a_0 is the contact radius, to be discussed later. The multiferroic MEE film is made of the magnetostrictive ($CoFe_2O_4$) and piezoelectric ($BaTiO_3$) phases whose material properties were from (Chen et al., 2010; Pan, 2001) with distinct s_k, as given in Table 1. The

rigid sphere is made of steel whose mass density ρ_s equals 7.85g/cm^3, which leads to the mass of the sphere, $M_s = 4\pi\rho_s R^3/3 = 3.29 \times 10^{-8}$g.

In one loading cycle of the velocity-induced MEE energy conversion, the loading velocity of the sphere increases from zero to the maximum, V_0, then decreases to zero following two loading types given in Eqs. (60) and (61). At the end of a loading cycle, the electric potential generated at the film surface was calculated. The working conditions of the MEE energy conversion are given in Table 2, showing that the term $M_s a^t$ in Eq. (64) is much smaller than P_0; Hence in the following numerical calculation, the effect of acceleration a^t on the contact behaviors are ignored.

Table 1. Material properties of the transversely isotropic multiferroic $BaTiO_3$-$CoFe_2O_4$ (Chen et al., 2010; Pan, 2001). (c_{ij} in 10^9N/m^2, e_{ij} in C/m^2, d_{ij} in N/(Am), ε_{ij} in 10^{-9}C^2/(Nm^2), μ_{ij} in 10^{-6}Ns^2/C^2).

c_{11}	c_{12}	c_{13}	c_{33}	c_{44}	c_{66}
226	125	124.25	216	44.15	50.5
e_{31}	e_{33}	e_{15}	d_{31}	d_{33}	d_{15}
-2.2	9.3	5.8	290.15	350	275
ε_{11}	ε_{33}			μ_{11}	μ_{33}
5.64	6.35			297.5	83.5

Table 2. Working conditions of the MEE energy conversion ($\xi_{11} = 2.03552 \times 10^{-12}\mathrm{m}^2/N$, $\xi_{12} = 1.77480 \times 10^{-3}\mathrm{m}^2/C$, and $\xi_{13} = 1.93900 \times 10^{-6}\mathrm{mA/N}$ are calculated from current material properties (Chen et al., 2010); an applied force of $P_0 = 1.8 \times 10^{-4}N$ is selected as a reference value).

Loading velocity c_0 ($c_0 = V_0/\sqrt{c_{44}/\rho}$)	0.4, 0.6, 0.8	Sphere radius R_0	1×10^{-6}m
Sphere radius R	$1.0R_0$, $2.0R_0$, $3.0R_0$	Contact radius a_0	$a_0 = \sqrt[3]{0.75\pi\xi_{11}R_0P_0}$
Film thickness h_t	$1.0a_0$, $2.0a_0$, $5.0a_0$	Indentation depth δ_0	a_0^2/R_0
Loading time at one cycle T_{total}	$0.8\delta_0/c_{sw}$	Contact pressure p_0	$2a_0/(\pi^2\xi_{11}R_0)$
Magnetic potential φ_0	$\xi_{13}\delta_0/\xi_{11}$	Electric potential ϕ_0	$\xi_{12}\delta_0/\xi_{11}$

3.1 Model verification and general MEE transient behaviors

3.1.1 Model verification

The model is verified through the comparison of the solutions from the present model at $h_t \to \infty$ & $V = 0$ with the corresponding analytical solutions from Chen et al. (2010), for the problem of a MEE half-space indented by a rigid insulating sphere of radius R=1×10^{-6}m under applied force P=2×10^{-4}N. The results are normalized by the maximum

pressure, p_0, the maximum electric potential, ϕ_0, the maximum magnetic potential, φ_0, and the contact radius, a_0, from the framework of solutions by Chen et al. (2010). The results in Fig. 3 (a-c) clearly reveal that the normalized contact pressure, surface electric potential, and surface magnetic potential well agree with those from reference (Chen et al., 2010).

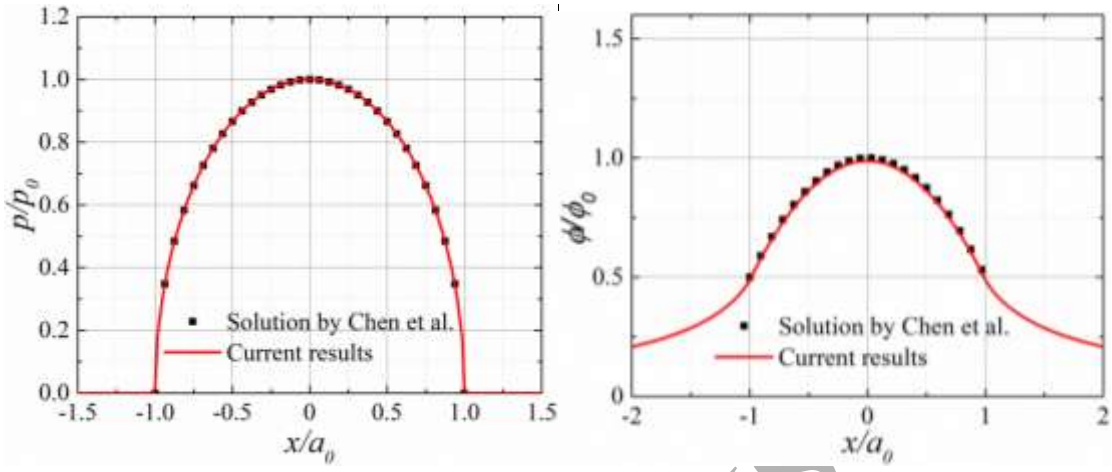

(a) (b)

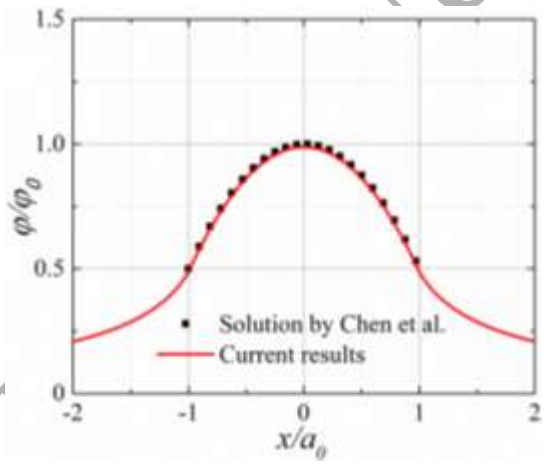

(c)

Fig. 3. Verification of the present model through degeneration to a half space and the comparison of the numerical results with the corresponding analytical solutions from Chen et al. (2010), for the problem of a MEE half-space indented by a rigid insulating sphere of radius R=1×10^{-6}m under applied force P=2×10^{-4}N: (a) normalized contact pressure p/p_0; (b) normalized surface electric potential ϕ/ϕ_0; (c) normalized surface magnetic potential φ/φ_0.

The model is further verified through the comparison of the present numerical results by letting $V = 0$ with the corresponding numerical results from our previous work (Zhang et al., 2017), for the problem of a MEE film indented by a rigid insulating sphere of radius R=1×10^{-6}m under applied force P=2×10^{-4}N. Three film thicknesses, h_t=1.0a_0, 2.0a_0, and 5.0a_0, are selected as examples. Figure 4 (a) shows the normalized contact pressure distributions, p/p_0, with respect to h_t, while (b) and (c) plot the surface electric potential distributions, ϕ/ϕ_0, and surface magnetic potential distributions, φ/φ_0. Clearly, p/p_0, ϕ/ϕ_0, and φ/φ_0

from the present method well agree with those from reference (Zhang et al., 2017).

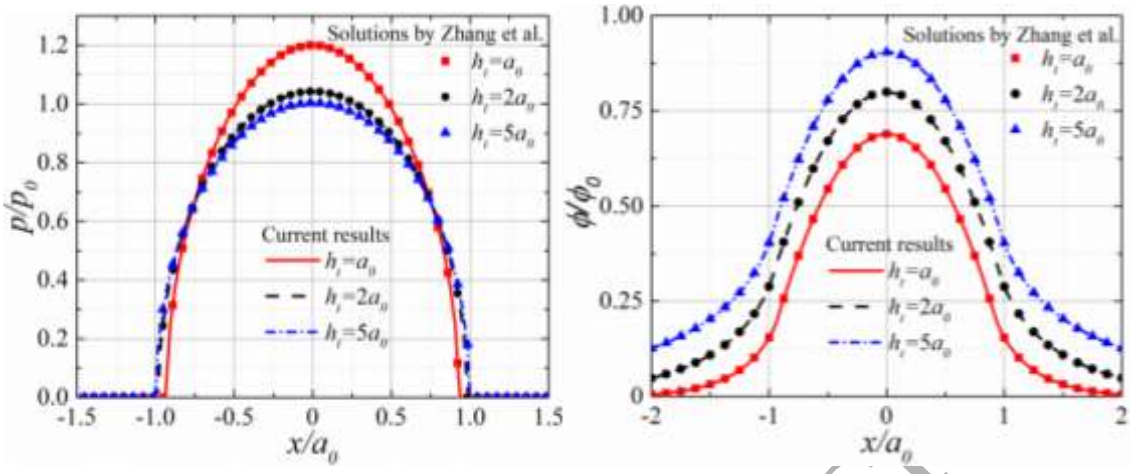

(a) (b)

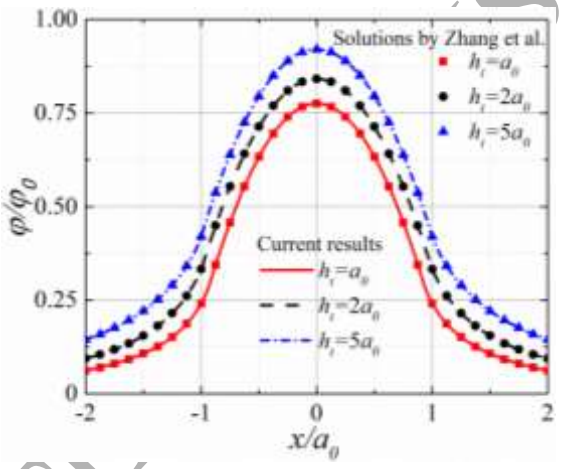

(c)

Fig. 4. Verification of the present model through degeneration with V=0 and the comparison of the numerical results with those from (Zhang et al., 2017), for the problem of a MEE film indented by a rigid insulating sphere of radius R=1×10^{-6}m under applied force P=2×10^{-4}N: (a) normalized contact pressure p/p_0; (b) normalized surface electric potential ϕ/ϕ_0; (c) normalized surface magnetic potential φ/φ_0.

3.1.2 General MEE transient behaviors

The model is first implemented to study the general MEE transient behaviors for the problem of a MEE film of h_t=1.0a_0 indented by a rigid insulating sphere of radius R=1×10^{-6}m under the applied force of P=2×10^{-4}N. Four constant velocities, c=0, 0.4, 0.6 and 0.8, are selected as examples. Figure 5 shows the effects of the loading velocity c on the general MEE transient behaviors, where (a), (b) and (c) are for the normalized contact pressure distributions, p/p_0, the surface electric potential distributions, ϕ/ϕ_0, and surface magnetic potential distributions, φ/φ_0, respectively. The contact pressure is relieved with the

increasing loading velocity of the sphere, which is also observed in (Zhou and Lee, 2012b) for the contact of a MEE half-plane indented by a moving cylindrical punch. The results show that a larger c leads to higher surface electric potentials ϕ/ϕ_0 and surface magnetic potentials, φ/φ_0.

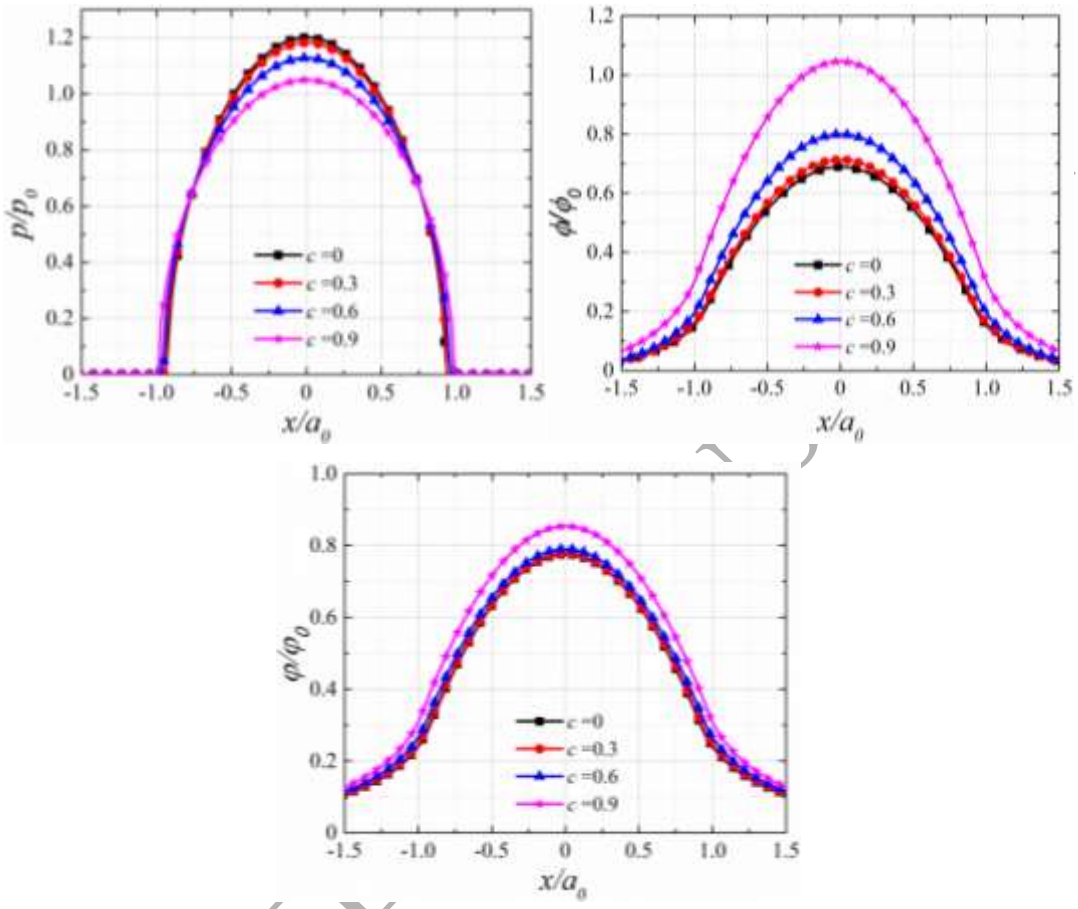

Fig. 5. General MEE transient behaviors, for the MEE film of h_t=1.0a_0 indented by a rigid insulating sphere of radius R=1×10^{-6}m under the applied force of P=2×10^{-4}N, for different velocity values of c=0, 0.4, 0.6 and 0.8: (a) normalized contact pressure p/p_0; (b) normalized surface electric potential ϕ/ϕ_0; and (c) normalized surface magnetic potential φ/φ_0.

3.2 Dynamic characterization of surface MEE contact behaviors

3.2.1 Effects of loading velocity on contact behaviors

The dynamic contact behaviors of the multiferroic film can be characterized by a transient indentation of a rigid insulating sphere under an increasing applied force $P(t)$ along the z axis. Figure 6 shows the types of loading velocity, where (a) and (b) are for the velocities of triangular and sinusoidal shapes, respectively. The influence of loading velocity on the dynamic contact behaviors is explored, while the film thickness is h_t=1.0a_0 and the sphere radius is R=1.0R_0 without losing generality. The total loading time T_{total} and indentation depth δ are fixed, for which c_0 should be carefully selected to satisfy the same indentation depth δ. Hence, for the velocity of triangular shape, maximum value c_0=0.4, 0.6

and 0.8 are selected while maximum value c_0=0.4·π/4, 0.6·π/4 and 0.8·π/4 are chosen for the velocities in sinusoidal variations. Figure 7 shows the dynamic contact behaviors with respect to increasing loading time for different c_0 and velocity types, where (a), (b), (c) and (d) plot the applied force P, normalized pressure p/p_0 at the contact center, maximum values of normalized electric potential ϕ/ϕ_0 and magnetic potential φ/φ_0, respectively. In general, a larger c_0 leads to larger contact characteristic values. Furthermore, these characteristic items under the triangular contact variation are slightly smaller than those under the sinusoidal contact variation in the early stage of the loading cycle, while the trend reverses in the later stage.

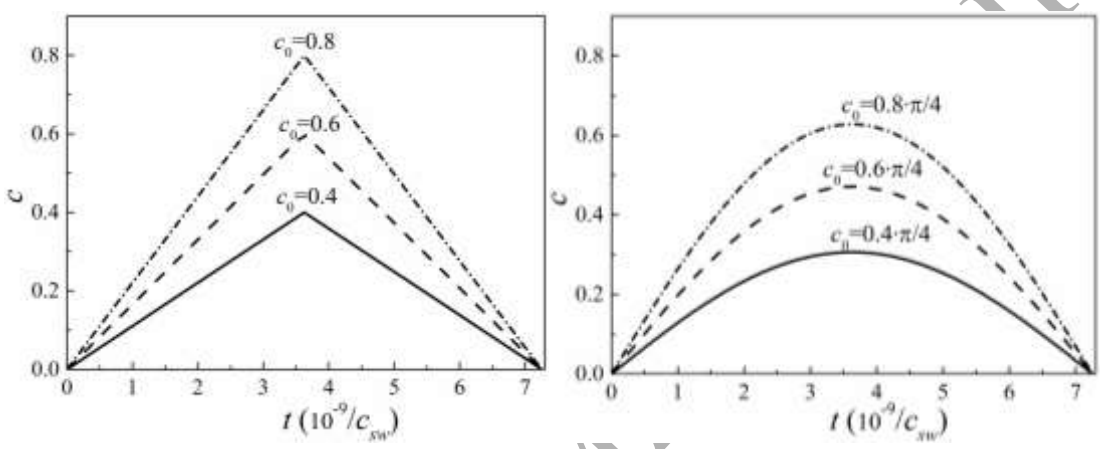

(a) (b)

Fig. 6. Types of loading velocity: (a) velocity of triangular shape; (b) velocity of sinusoidal shape. c_0 is the maximum value of the velocity. Note that the areas under corresponding curves are the same

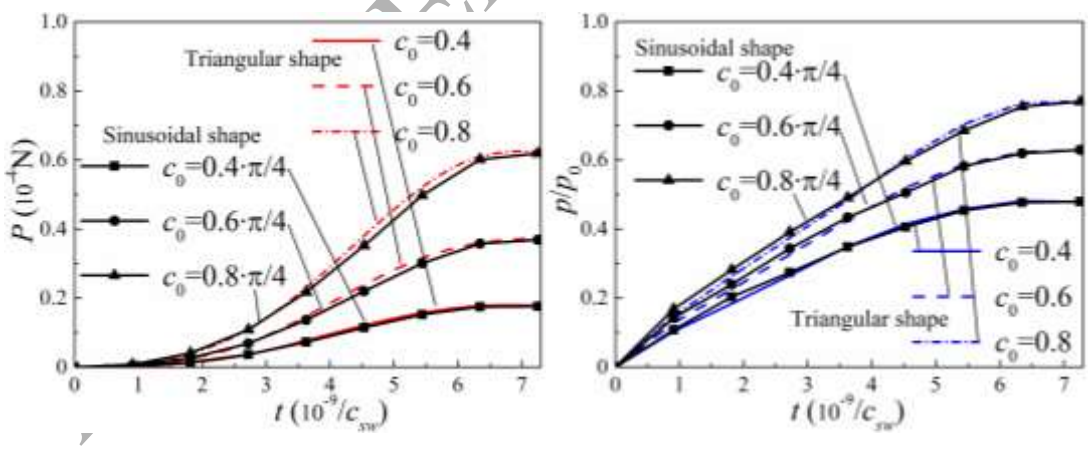

(a) (b)

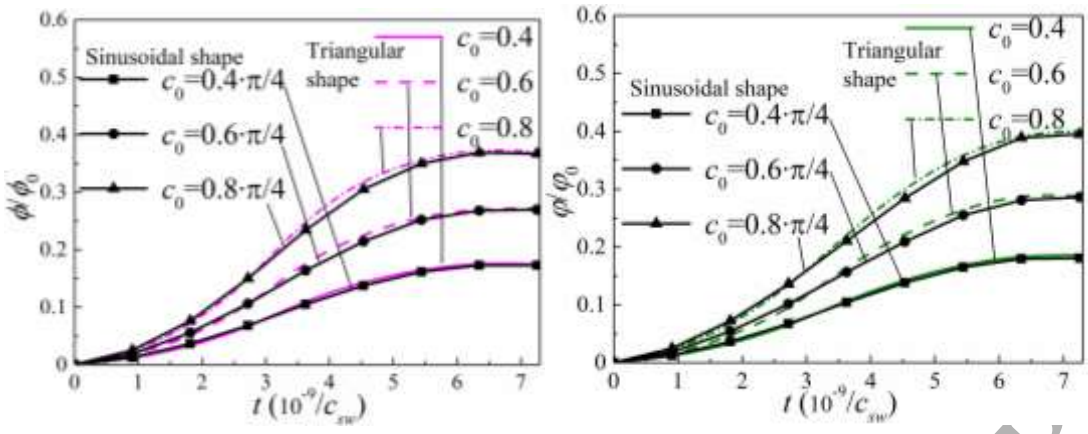

(c) (d)

Fig. 7. Dynamic contact behaviors for different values of maximum velocity c_0: (a) applied force P; (b) normalized pressure p/p_0 at the contact center; (c) maximum values of normalized electric potential ϕ/ϕ_0; (d) maximum values of normalized magnetic potential φ/φ_0.

3.2.2 Effects of the MEE film thickness on contact behaviors

The same problem is investigated for the MEE film with different thicknesses h_t=1.0a_0, 2.0a_0, 5.0a_0, and the sphere radius of R=1.0R_0. Because Fig. 7 confirms that the loading velocity types have negligible influences on contact behaviors, the triangular velocity with maximum value c_0=0.8 is selected for these analyses. Figure 8 shows the results with respect to increasing loading time for different film thickness h_t, where (a), (b), (c) and (d) plot the applied force P, normalized pressure p/p_0 at the contact center, and the maximum values of normalized electric potential ϕ/ϕ_0 and magnetic potential φ/φ_0, respectively. Obviously, the applied force and the maximum values of the contact pressure decrease with increasing film thickness h_t. On the other hand, a thicker film thickness leads to a larger electric/magnetic potential at the contact center.

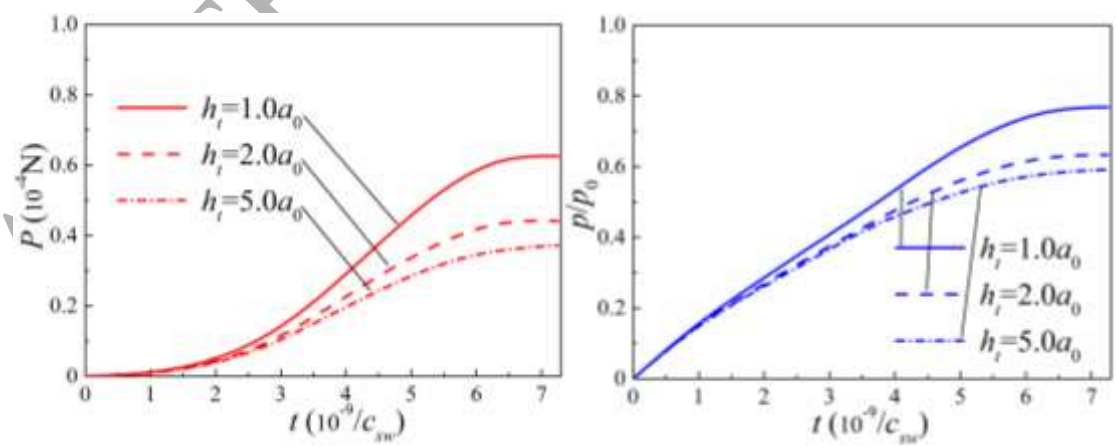

(a) (b)

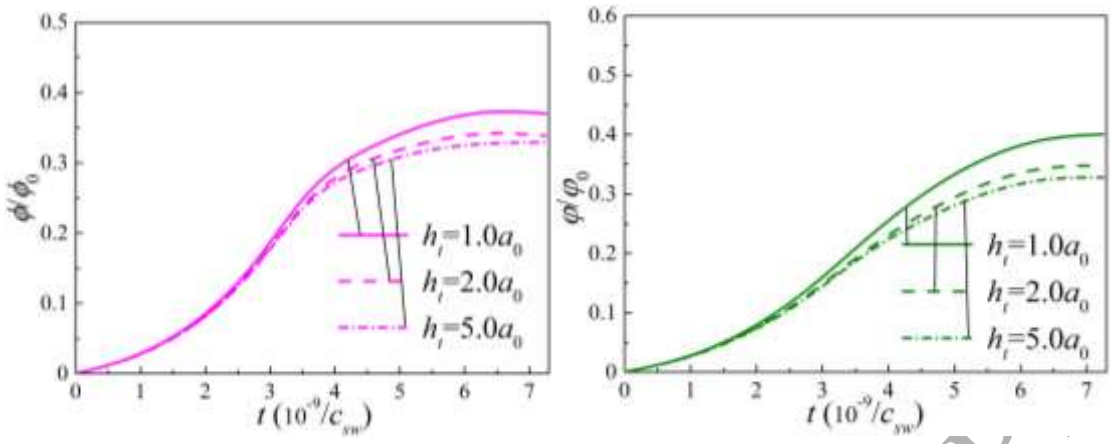

(c) (d)

Fig. 8. Dynamic contact behaviors of the MEE films with different thicknesses, h_t: (a) applied force P; (b) normalized pressure p/p_0 at the contact center; (c) maximum values of normalized electric potential ϕ/ϕ_0; (d) maximum values of normalized magnetic potential φ/φ_0. Results are obtained from the velocity of the triangular shape.

3.2.3 Effects of sphere radius on the contact behaviors

In this section, the dynamic contacts of the MEE film thickness of h_t=1.0a_0 with the rigid insulating spheres of different sizes, R=1.0R_0, 2.0R_0 and 3.0R_0, are analyzed under the same triangular velocity with c_0=0.8 mentioned before. Figure 9 shows the dynamic contact behaviors of the MEE thin film with respect to increasing loading time for different sphere radius R, where sets (a), (b), (c) and (d) plot the applied force P, normalized pressure p/p_0 at the contact center, maximum values of normalized electric potential ϕ/ϕ_0 and magnetic potential φ/φ_0, respectively. Clearly, increasing sphere radius R causes the applied force to increase, but the maximum values of the contact pressure decreases. On the other hand, a larger sphere radius leads to a higher electric/magnetic potential at the contact center.

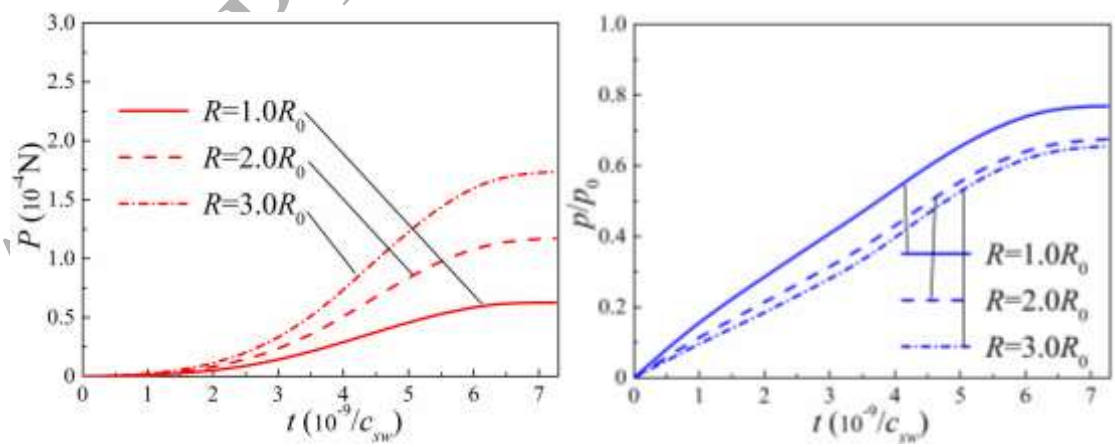

(a) (b)

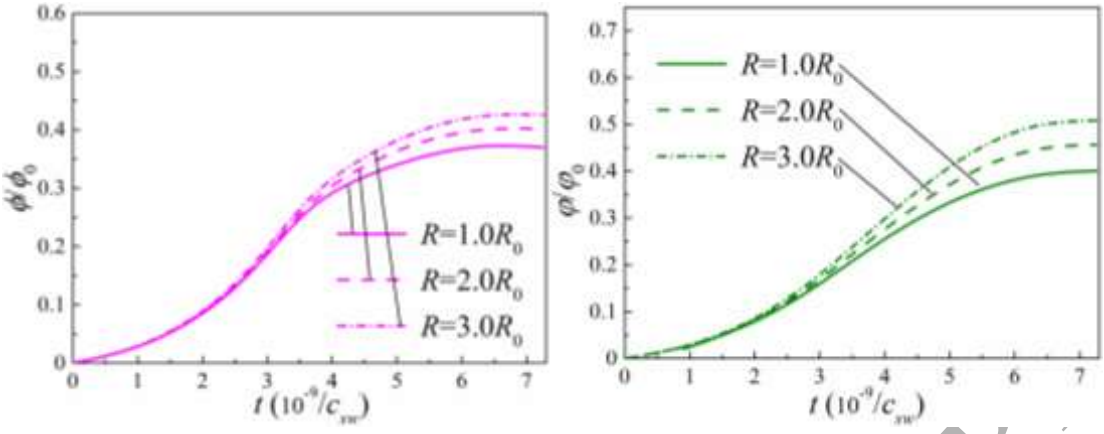

(c) (d)

Fig. 9. Dynamic contact behaviors influenced by sphere radius R: (a) applied force P; (b) normalized pressure p/p_0 at the contact center; (c) maximum values of normalized electric potential ϕ/ϕ_0; (d) maximum values of normalized magnetic potential φ/φ_0. Results are obtained from the triangular velocity..

3.3 Sub-surface stress analysis

The von Mises stress is important to understand the plastic behaviors of the materials under dynamic contact, which is defined by

$$\sigma_s = \sqrt{[(\sigma_{xx}-\sigma_{yy})^2+(\sigma_{yy}-\sigma_{zz})^2+(\sigma_{zz}-\sigma_{xx})^2+6(\sigma_{xy}^2+\sigma_{xz}^2+\sigma_{yz}^2)]/2}. \qquad (65)$$

Figure 10(a) plots the distributions of the von Mises stress along the z-axis in the MEE film, for the problem of triangular velocity with c_0=0.6, film thickness h_t=1.0a_0, and sphere radius R=1.0R_0. The insets display the contours of the von Mises stress σ_s/p_0 in the x-z section for time t=7.2532. As loading time t increases, the values of the stress become larger, and the location of the maximum von Mises stress departs further away from the contact surface. It is found that t=3.6266, corresponding to peak velocity c_0=0.6, leads to a significant sudden change in the von Mises stress, as shown in Fig. 10(a). In order to understand this phenomenon, the distributions of the von Mises stress caused by the sinusoidal loading velocity with c_0=0.6 are plotted in Fig. 10(b) for comparison, in which similar sudden changes are found in the curves for velocity c=0.5543 at t=2.7200, for velocity c=0.6 at t=3.6266, and for velocity c=0.5543 at t=4.5332. Besides, the distributions of the von Mises stress for the problem of triangular velocity with c_0=0.4 is plotted in Fig. 10(c), where the sudden change vanishes. Furthermore, the distributions of the von Mises stress at t=3.6266 for the problem of triangular-shape loading velocity with different peak velocity c_0=0.4, 0.45, 0.5, 0.55 and 0.6 are plotted in Fig. 10(d), revealing that the loading velocity is responsible of sudden change in the von Mises stress along the z direction, and that this sudden change becomes more significant if the peak velocity c_0 is higher.

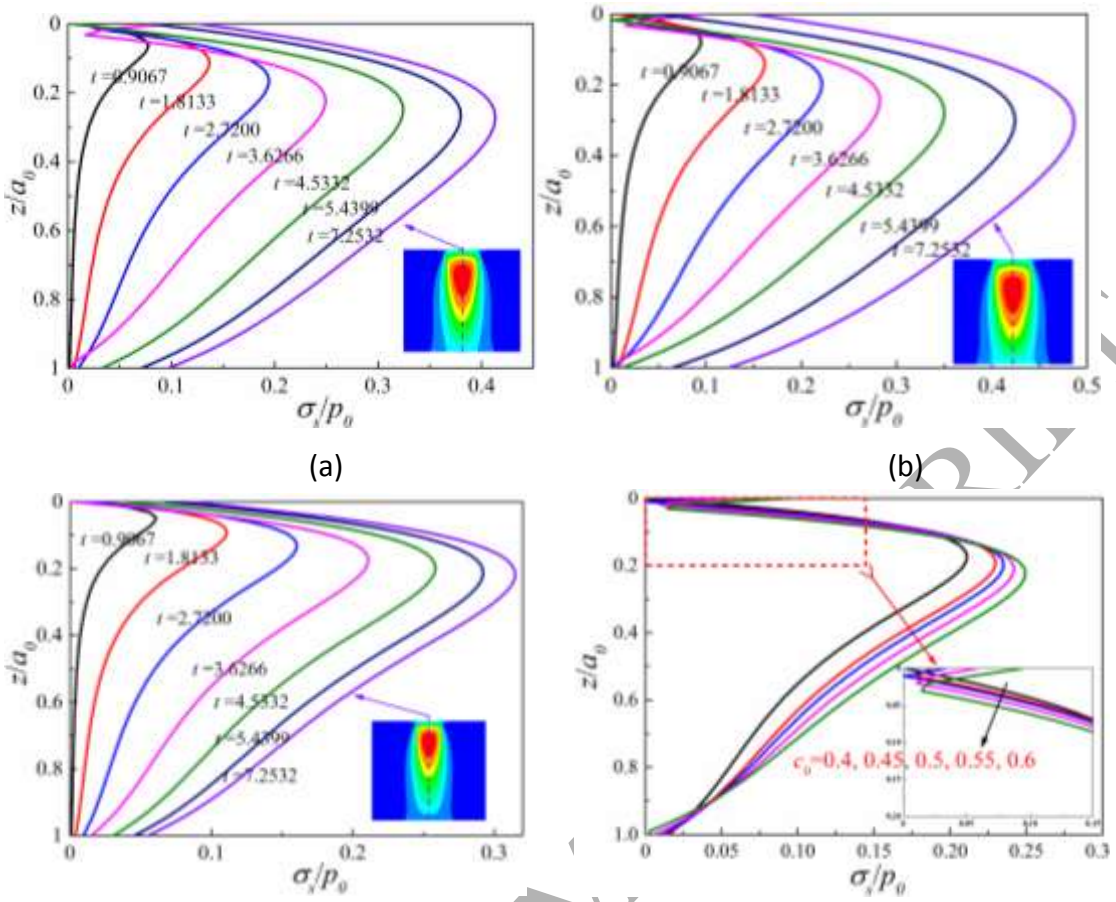

(a) (b)

(c) (d)

Fig. 10. Distributions of the von Mises stress along the z-axis in the MEE film: (a) c_0=0.6 for the triangular-shape loading velocity, (b) c_0=0.6 for the sinusoidal-shape loading velocity, (c) c_0=0.4 for the triangular-shape loading velocity, (d) at t=3.6266 under the triangular-shape loading velocity with different peak velocities c_0=0.4, 0.45, 0.5, 0.55 and 0.6. Film thickness h_t=1.0a_0, and sphere radius R=1.0R_0. The insets display the contours of the von Mises stress σ_s/p_0 in the *x-z* section for time t=7.2532.

The variations of the maximum values of σ_s/p_0 with loading time t are plotted in Fig. 11 for clarity. The insets display the contours of the von Mises stress σ_s/p_0 in the *x-z* section at different loading time t. The maximum value of σ_s/p_0 increases with time. A thicker film results in a smaller value of σ_s/p_0, as shown in Fig. 11 (a). On the other hand, a smaller sphere radius R induces a larger value of σ_s/p_0, as shown in Fig. 11 (b).

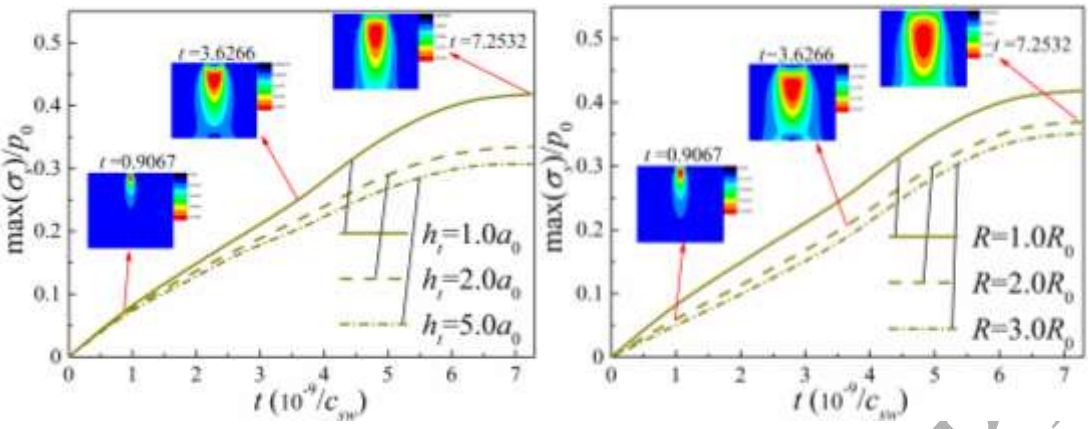

(a) (b)

Fig. 11. Variations of the maximum values of σ_s/p_0 with loading time *t* due to the triangular-shape loading velocity: (a) for the MEE film of different thickness h_t=1.0a_0, 2.0a_0 and 5.0a_0; (b) for different sphere radius R=1.0R_0, 2.0R_0 and 3.0R_0. Loading velocity c_0=0.6, sphere radius R=1.0R_0. The insets display the contours of the von Mises stress σ_s/p_0 in the *x-z* section for time *t*=0.9067, 3.6266 and 7.2532.

3.4 Energy conversion performance

Sun and Kim (2010) proposed an energy conversion factor to evaluate the performance of MEE energy conversion as a natural extension of the work by Zheng et al. (2009) on piezoelectric energy harvest. Inspired by their study, the work W^P done by the applied force *P* is stored in the forms of strain energy Π^S, electric energy Π^E, magnetic energy Π^M, piezoelectric energy Π^{PE}, piezomagnetic energy Π^{PM}, and magnetoelectric energy Π^{ME}, which can be expressed as follows without considering thermal and plastic losses:

$$\Pi^S = \frac{1}{2}\int \gamma_{ij}^T c_{ijkl}\gamma_{kl}\mathrm{d}V, \quad \Pi^E = \frac{1}{2}\int E_i^T \varepsilon_{ij} E_j \mathrm{d}V, \quad \Pi^M = \frac{1}{2}\int H_i^T \mu_{ij} H_j \mathrm{d}V,$$
$$\Pi^{PE} = \frac{1}{2}\int \gamma_{ij}^T e_{ijk} E_k \mathrm{d}V, \quad \Pi^{PM} = \frac{1}{2}\int \gamma_{ij}^T d_{ijk} H_k \mathrm{d}V, \quad \Pi^{ME} = \frac{1}{2}\int E_i^T g_{ij} H_j \mathrm{d}V. \tag{65}$$

Furthermore, the work, W^P, done by the applied force, *P*, can be written as

$$W^P = P \cdot \delta, \tag{66}$$

where δ denotes the indentation depth of the rigid sphere on the MEE film by the applied force *P*.

Therefore, the energy conversion factor η_E from mechanical energy to electric energy (we call it electric energy conversion factor later) can be defined as

$$\eta_E = \frac{\Pi^E}{W^P}. \tag{67}$$

In this study, we are focusing on the evaluation of the performance of the MEE film-based energy converter, in which the MEE film can be described as an energy converter to utilize the electric potential to drive the electron flow through the circuit, rather than exactly determining the amount of the generated electric energy. The finite element analysis by Xu and Qin (2017) shows the electric potential linearly varies along the length direction of the nanowires. Reasonably, assuming the electric potential linearly varies along the *z* axis of the MEE film, and the electric energy Π^E can be approximately calculated by,

$$\Pi^E = \frac{1}{2h_t}\int \bar{\phi}\cdot\varepsilon_{33}\cdot\bar{\phi}\,\mathrm{d}A_c, \tag{68}$$

where $\bar{\phi}$ represents the electric potential at the top surface of the MEE film, A_c is the in-plane (*x*-*y* section) area of the interaction domain. The electric potential in the lower surface of the MEE film is zero due to its grounding.

Figure 12 shows the electric energy conversion factor η_E with respect to varying film thickness and sphere radius, for the problem of triangular loading velocity with c_0=0.6. Clearly, a thicker film h_t results in a smaller value of η_P. On the other hand, a smaller sphere radius *R* induces a larger value of η_E.

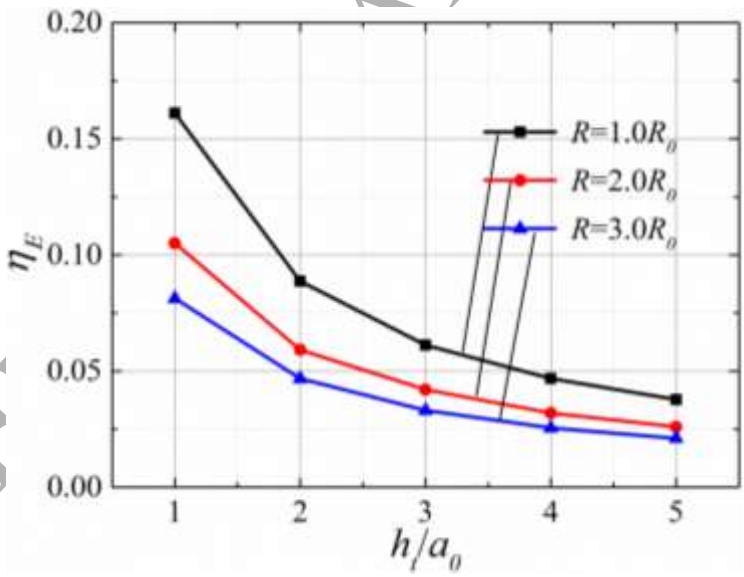

Fig. 12. Variation of the electric energy conversion factor η_E with respect to film thickness and sphere radius, for the problem of triangular loading velocity of c_0=0.6.

Figure 12 offers an optimization design scheme for the overall electric energy conversion efficiency with respect to film thickness and indenter size. Another critical issue is how the efficiency can be improved from material design. The material properties listed in Table 1 has 16 independent constituent constants, including six elastic stiffnesses c_{ij}, three piezoelectric coefficients e_{ij}, three piezomagnetic coefficients d_{ij}, two dielectric permittivities

ε_{ij}, and two magnetic permeabilities μ_{ij}. It is important to evaluate coupling effects and dependence of the electric energy conversion factor η_E on those material properties. Furthermore, the magnetic energy conversion factor $\eta_M = \Pi^M / W^P$ is also calculated for the connection between the electric and magnetic energies. The sensitivity function suggested by Makagon et al. (2007), (2009) is employed to evaluate the coupling effects of those material properties on the energy conversion rate. The dimensionless sensitivity below is numerically calculated with the step length of $0.01f^0$:

$$S(f) = \frac{\eta\big|_{f=1.01f^0} - \eta\big|_{f=0.99f^0}}{0.02\eta\big|_{f=f^0}} \tag{69}$$

where f is a selected material constant with f^0 being its reference value. η is an energy conversion factor, which can be electric energy conversion factor η_E, and magnetic energy conversion factor η_M.

Figure 13 plots the sensitivities of energy conversion factors, η_E and η_M, to the 16 independent material constants, for the problem of film thickness h_t=1.0a_0, sphere radius R=1.0R_0, and triangular loading velocity of c_0=0.6. The energy conversion factors show obvious dependences on the elastic stiffnesses c_{11}, c_{13}, c_{33}, c_{44}, dielectric permittivity ε_{11}, piezoelectric coefficients e_{33}, e_{15}, piezomagnetic coefficients d_{ij}, and magnetic permeability μ_{11}, but they are less sensitive to elastic constant c_{12}, piezoelectric coefficient e_{31}, dielectric permittivity ε_{33}, and magnetic permeability μ_{33}. c_{11}, c_{13}, e_{33}, and e_{15} promote the electric energy conversion from mechanical energy to electric energy while c_{33}, c_{44} and ε_{11} tend to confine the electric energy conversion. Besides, c_{11}, d_{33}, and d_{15} promote the increase in magnetic energy conversion from mechanical energy while c_{13}, c_{33}, c_{44}, e_{33}, e_{15}, d_{31}, and μ_{11} tend to reduce the magnetic energy conversion. The above observations are stated in details below, which are consistent with the physical nature and the reported publications for the current problems.

(i) For larger tangential dielectric permittivity ε_{11} and magnetic permeability μ_{11}, the dielectric and magnetic effects spread much more laterally, which reduce the electric/magnetic energy generations at the contact center. On the other hand, for larger normal dielectric permittivity ε_{33} and magnetic permeability μ_{33}, the dielectric and magnetic effects are concentrated beneath the contact center, which makes the electric/magnetic energy generations larger. But those increases in electric/magnetic energy are not very significant when compared to the reduced amounts of electric/magnetic energy due to the influences of ε_{11} and μ_{11}. Therefore, dielectric permittivities and magnetic permeabilities can be singled out for their abilities to reduce the efficiency of the energy conversion, which are in agreement with the observations reported in most publications about piezoelectric/magnetoelectric issues (Umeda et al., 1996, 1997; Zhang et al., 2018).

(ii) It was reported in (Sodano et al., 2004) that the efficiency of electric energy conversion increased with the increasing piezoelectric coefficients. In the numerical results presented in Fig. 13, piezoelectric coefficient e_{33} results in more prominent contribution to the electric energy conversion. Furthermore, piezomagnetic coefficient d_{33} remarkably enhance the performance of the magnetic energy conversion. For larger e_{33} and d_{33}, the electromechanical coupling and magnetomechanical coupling become stronger, which enhances the electric/magnetic behaviors even when the system is under the same mechanical characteristics.

(iii) Elastic constant c_{12} has a negligible influence on the MEE behavior, as evidenced in our previous research (Zhang et al., 2018). c_{11}, c_{33}, and c_{44} have the same influences on η_E and η_M, in which c_{11} tends to promote the efficiency of energy conversion while c_{33} and c_{44} tend to reduce the efficiency. However, c_{13} has a positive effect on η_E but a negative effect on η_M. As reported in (Wang and Chen, 2011), the equivalent Young's modulus E_0 and Poisson's ratio υ_0 in the plane of isotropy can be calculated by $E_0 = (c_{11}^2 c_{33} - 2c_{11}c_{13}^2 - c_{12}^2 c_{33} + 2c_{12}c_{13}^2)/(c_{11}c_{33} - c_{13}^2)$, and $\upsilon_0 = (c_{12}c_{33} - c_{13}^2)/(c_{11}c_{33} - c_{13}^2)$. If υ_0 is constant, c_{11} tends to increase the equivalent Young's modulus E_0, which makes the apparent normal stiffness stronger and then promotes larger electric/magnetic energy conversions from the mechanical energy. On the other hand, in order to keep υ_0 constant and increase E_0 as stated above, c_{33} should decrease its value, which indicates an effect totally opposite to that of c_{11}.

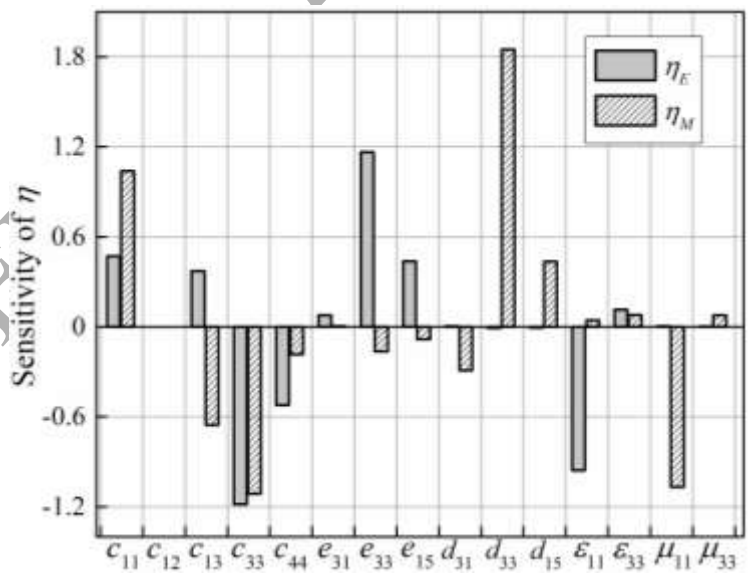

Fig. 13. Sensitivity of energy conversion factors η_E and η_M to the 16 independent material constants, for the problem of film thickness h_t=1.0a_0, sphere radius R=1.0R_0, and triangular loading velocity of c_0=0.6.

4. Conclusions

The theoretical base and a semi-analytical model (SAM) for simulating the dynamic

contact of a rigid sphere and the surface of a multiferroic magnetoelectroelastic (MEE) film under transient applied force has been developed. The research has yielded analytical frequency response functions (FRFs) and their conversion into influence coefficients (ICs) for the MEE film subjected to a set of generalized normal force and generated surface electric/magnetic charges under the influence of changing loading velocity in a dynamic process. The research has also further developed the fast numerical techniques, such as the conjugate gradient method (CGM) and the fast Fourier transform (FFT), for efficient numerical solutions to the dynamic contact behaviors of the thin-film material, including the distributions and variations of contact pressure and electric/magnetic potentials, as well as subsurface stresses. The combined influences of loading velocity, film thickness, and sphere radius on the dynamic MEE responses have been investigated, and the numerical results lead to the following conclusions.

1). The dynamic contact characteristics, including the applied force and electric/magnetic potentials under the triangular loading speed variation are slightly smaller than those under the sinusoidal loading velocity variation in the early stage of the loading cycle, while the trend reverses in the later stage. The contact characteristic values increase with the maximum velocity and sphere radius, but decrease with film thickness.

2). The von Mises stress become larger and the location of the maximum von Mises stress departs further away from the contact surface as loading velocity increases in one loading cycle. A thicker film results in a smaller stress. On the other hand, a larger sphere radius induces a smaller stress under the same peak velocity.

3). An energy conversion factor is employed to evaluate the performance of MEE energy conversion. Under the same load and loading velocity, thicker film results in a lower energy conversion from mechanical energy to electric energy. On the other hand, a smaller sphere radius promotes a larger electric energy conversion.

4). The sensitivity analyses of the energy conversion factors with respect to material properties show obvious their dependences on elastic stiffnesses c_{11}, c_{13}, c_{33}, c_{44}, dielectric permittivity ε_{11}, piezoelectric coefficient e_{33}, e_{15}, piezomagnetic coefficients d_{ij}, and magnetic permeability μ_{11}, but they are less sensitive to elastic constant c_{12}, piezoelectric coefficient e_{31}, dielectric permittivity ε_{33}, and magnetic permeability μ_{33}. Dielectric permittivities and magnetic permeabilities can be singled out for their abilities to reduce the efficiency of the energy conversion. Piezoelectric coefficient e_{33} results in more prominent contribution to the electric energy conversion. Furthermore, piezomagnetic coefficient d_{33} remarkably enhance the performance of the magnetic energy conversion. Elastic stiffness c_{11} tends to

promote the efficiency of energy conversion while c_{33} and c_{44} could reduce the efficiency. However, c_{13} has a positive effect on electric energy conversion but a negative effect on magnetic energy conversion. These results offer references to optimal material designs towards high efficiency of different energy conversions.

Above all, the numerical results in this paper have answered the key questions listed in the introduction, which are (a) the contact characteristics in terms of electric/magnetic potentials, contact pressure, and stresses are all much dependent on the dynamic contact loading. (b) The contact characteristic values increase with the peak velocity, and the variations in loading velocity significantly affect the mechanical and electric/magnetic responses, as stated in conclusion 1). (c) The sensitivity analyses of material properties show obvious coupling effects and dependence of electric energy conversion on several material properties, as stated in conclusion 4). In order to improve the efficiency of mechanical-electrical/magnetic energy conversions, a systematic optimization can be developed from the structural topology and material components, based on conclusion 3) and 4).

Acknowledgments

The authors would like to acknowledge the supports from Northwestern's Center for Surface Engineering and Tribology and National Nature Science Foundation of China under grants 51775458, 11672252, and 51775457, and the fellowship award to Xin Zhang from China Scholarship Council.

Appendix A

The constants in Eq. (22) are given as follows,

$$
\begin{aligned}
&n_0 = b_1 + b_{10}c_{44}c^2 + b_{11}c_{44}^2c^4,\\
&n_1 = b_2 + b_7c_{44}c^2 + b_9c_{44}^2c^4,\\
&n_2 = b_3 + b_5c_{44}^2c^4 + b_8c_{44}c^2,\\
&n_3 = b_4 + b_6c_{44}c^2,\\
&n_4 = c_{11}[c_{44}(\varepsilon_{11}\mu_{11} - g_{11}^2) - 2e_{15}g_{11}d_{15} + \mu_{11}e_{15}^2 + \varepsilon_{11}d_{15}^2],
\end{aligned}
\tag{A.1}
$$

where

$$
b_1 = c_{44}[(c_{33}(\varepsilon_{33}\mu_{33} - g_{33}^2) - 2e_{33}g_{33}d_{33} + \mu_{33}e_{33}^2 + \varepsilon_{33}d_{33}^2], \tag{A.2}
$$

$$
\begin{aligned}
b_2 = {} & c_{11}[c_{33}(\varepsilon_{33}\mu_{33} - g_{33}^2) - 2e_{33}g_{33}d_{33} + \mu_{33}e_{33}^2 + \varepsilon_{33}d_{33}^2] \\
& + c_{44}[c_{44}(\varepsilon_{33}\mu_{33} - g_{33}^2) + c_{33}(\varepsilon_{11}\mu_{33} + \varepsilon_{33}\mu_{11} - 2g_{11}g_{33}) \\
& - 2e_{15}g_{33}d_{33} - 2e_{33}(g_{11}d_{33} + g_{33}d_{15}) + (\mu_{11}e_{33}^2 + 2\mu_{33}e_{15}e_{33}) \\
& + (\varepsilon_{11}d_{33}^2 + 2\varepsilon_{33}d_{15}d_{33})] - (c_{13} + c_{44})[(c_{13} + c_{44})(\varepsilon_{33}\mu_{33} - g_{33}^2) \\
& + (e_{15} + e_{31})(e_{33}\mu_{33} - d_{33}g_{33}) - (d_{15} + d_{31})(e_{33}g_{33} - d_{33}\varepsilon_{33})] \\
& - (e_{15} + e_{31})[(c_{13} + c_{44})(e_{33}\mu_{33} - g_{33}d_{33}) - (e_{15} + e_{31})(c_{33}\mu_{33} + d_{33}^2) \\
& + (d_{15} + d_{31})(c_{33}g_{33} + d_{33}e_{33})] - (d_{15} + d_{31})[(c_{13} + c_{44})(\varepsilon_{33}d_{33} - e_{33}g_{33}) \\
& + (e_{15} + e_{31})(c_{33}g_{33} + e_{33}d_{33}) - (d_{15} + d_{31})(c_{33}\varepsilon_{33} + e_{33}^2)],
\end{aligned}
\tag{A.3}
$$

$$
\begin{aligned}
b_3 = {} & c_{11}[c_{44}(\varepsilon_{33}\mu_{33} - g_{33}^2) + c_{33}(\varepsilon_{11}\mu_{33} + \varepsilon_{33}\mu_{11} - 2g_{11}g_{33}) \\
& - 2e_{15}g_{33}d_{33} - 2e_{33}(g_{11}d_{33} + g_{33}d_{15}) + (\mu_{11}e_{33}^2 + 2\mu_{33}e_{15}e_{33}) \\
& + (\varepsilon_{11}d_{33}^2 + 2\varepsilon_{33}d_{15}d_{33})] + c_{44}[c_{44}(\varepsilon_{11}\mu_{33} + \varepsilon_{33}\mu_{11} - 2g_{11}g_{33}) \\
& + c_{33}(\varepsilon_{11}\mu_{11} - g_{11}^2) - 2e_{15}(g_{11}d_{33} + g_{33}d_{15}) \\
& - 2e_{33}g_{11}d_{15} + 2\mu_{11}e_{15}e_{33} + \mu_{33}e_{15}^2 + 2\varepsilon_{11}d_{15}d_{33} + \varepsilon_{33}d_{15}^2] \\
& - (c_{13} + c_{44})[(c_{13} + c_{44})(\varepsilon_{11}\mu_{33} + \varepsilon_{33}\mu_{11} - 2g_{11}g_{33}) \\
& + (e_{15} + e_{31})(e_{15}\mu_{33} + e_{33}\mu_{11}) - (e_{15} + e_{31})(d_{15}g_{33} + d_{33}g_{11}) \\
& - (d_{15} + d_{31})(e_{15}g_{33} + e_{33}g_{11}) + (d_{15} + d_{31})(d_{15}\varepsilon_{33} + d_{33}\varepsilon_{11})] \\
& - (e_{15} + e_{31})[(c_{13} + c_{44})(e_{15}\mu_{33} + e_{33}\mu_{11} - g_{11}d_{33} - g_{33}d_{15}) \\
& - (e_{15} + e_{31})(c_{44}\mu_{33} + c_{33}\mu_{11} + 2d_{15}d_{33}) \\
& + (d_{15} + d_{31})(c_{44}g_{33} + c_{33}g_{11} + d_{15}e_{33} + d_{33}e_{15})] \\
& - (d_{15} + d_{31})[(c_{13} + c_{44})(\varepsilon_{11}d_{33} + \varepsilon_{33}d_{15} - e_{15}g_{33} - e_{33}g_{11}) \\
& + (e_{15} + e_{31})(c_{44}g_{33} + c_{33}g_{11} + e_{15}d_{33} + e_{33}d_{15}) \\
& - (d_{15} + d_{31})(c_{44}\varepsilon_{33} + c_{33}\varepsilon_{11} + 2e_{15}e_{33})],
\end{aligned}
\tag{A.4}
$$

$$
\begin{aligned}
b_4 = {} & c_{11}[c_{44}(\varepsilon_{11}\mu_{33} + \varepsilon_{33}\mu_{11} - 2g_{11}g_{33}) + c_{33}(\varepsilon_{11}\mu_{11} - g_{11}^2) \\
& - 2e_{15}(g_{11}d_{33} + g_{33}d_{15}) - 2e_{33}g_{11}d_{15} + 2\mu_{11}e_{15}e_{33} + \mu_{33}e_{15}^2 \\
& + 2\varepsilon_{11}d_{15}d_{33} + \varepsilon_{33}d_{15}^2] + c_{44}[c_{44}(\varepsilon_{11}\mu_{11} - g_{11}^2) - 2e_{15}g_{11}d_{15} \\
& + \mu_{11}e_{15}^2 + \varepsilon_{11}d_{15}^2] - (c_{13} + c_{44})[(c_{13} + c_{44})(\varepsilon_{11}\mu_{11} - g_{11}^2) \\
& + (e_{15} + e_{31})(e_{15}\mu_{11} - d_{15}g_{11}) - (d_{15} + d_{31})(e_{15}g_{11} - d_{15}\varepsilon_{11})] \\
& - (e_{15} + e_{31})[(c_{13} + c_{44})(e_{15}\mu_{11} - g_{11}d_{15}) \\
& - (e_{15} + e_{31})(c_{44}\mu_{11} + d_{15}^2) + (d_{15} + d_{31})(c_{44}g_{11} + d_{15}e_{15})] \\
& - (d_{15} + d_{31})[(c_{13} + c_{44})(\varepsilon_{11}d_{15} - e_{15}g_{11}) \\
& + (e_{15} + e_{31})(c_{44}g_{11} + e_{15}d_{15}) - (d_{15} + d_{31})(c_{44}\varepsilon_{11} + e_{15}^2)],
\end{aligned}
\tag{A.5}
$$

$$
\begin{aligned}
b_5 &= \varepsilon_{11}\mu_{11} - g_{11}^2, \\
b_6 &= c_{44}g_{11}^2 + 2e_{15}d_{15}g_{11} + c_{11}g_{11}^2 - c_{44}\varepsilon_{11}\mu_{11} - d_{15}^2\varepsilon_{11} - e_{15}^2\mu_{11} - c_{11}\varepsilon_{11}\mu_{11},
\end{aligned}
\tag{A.6}
$$

ACCEPTED MANUSCRIPT

$$
\begin{aligned}
b_7 = {} & c_{44}g_{33}^2 - 2e_{15}e_{33}\mu_{33} + 2e_{15}d_{33}g_{33} + 2e_{33}d_{15}g_{33} + 2e_{31}d_{15}g_{33} + 2e_{31}d_{31}g_{33} \\
& - 2d_{15}d_{31}\varepsilon_{33} - c_{44}\varepsilon_{33}\mu_{11} - c_{44}\varepsilon_{11}\mu_{33} - c_{11}\varepsilon_{33}\mu_{33} - c_{33}\varepsilon_{11}\mu_{33} - c_{33}\varepsilon_{33}\mu_{11} \\
& - 2e_{15}e_{31}\mu_{33} + 2e_{15}d_{15}g_{33} + 2c_{44}g_{11}g_{33} + 2e_{15}d_{31}g_{33} + 2e_{33}d_{33}g_{11} - 2d_{15}d_{33}\varepsilon_{33} \\
& + 2c_{33}g_{11}g_{33} - c_{44}\varepsilon_{33}\mu_{33} - e_{31}^2\mu_{33} - d_{31}^2\varepsilon_{33} - d_{15}^2\varepsilon_{33} - e_{33}^2\mu_{11} - e_{15}^2\mu_{33} + c_{11}g_{33}^2 - d_{33}^2\varepsilon_{11},
\end{aligned}
\tag{A.7}
$$

$$
\begin{aligned}
b_8 = {} & -c_{44}\varepsilon_{33}\mu_{11} - c_{44}\varepsilon_{11}\mu_{33} + 2e_{15}d_{15}g_{33} + 2c_{44}g_{11}g_{33} - d_{15}^2\varepsilon_{33} - e_{15}^2\mu_{33} \\
& - c_{11}\varepsilon_{11}\mu_{33} - c_{11}\varepsilon_{33}\mu_{11} - c_{44}\varepsilon_{11}\mu_{11} - c_{33}\varepsilon_{11}\mu_{11} + 2e_{33}d_{15}g_{11} + 2c_{11}g_{11}g_{33} \\
& + 2e_{15}d_{33}g_{11} + 2e_{15}d_{31}g_{11} + 2e_{31}d_{15}g_{11} - 2d_{15}d_{33}\varepsilon_{11} + 2e_{31}d_{31}g_{11} - 2e_{15}e_{31}\mu_{11} \\
& - 2e_{15}e_{33}\mu_{11} + 2e_{15}d_{15}g_{11} - 2d_{15}d_{31}\varepsilon_{11} + c_{33}g_{11}^2 + c_{44}g_{11}^2 - e_{15}^2\mu_{11} - d_{31}^2\varepsilon_{11} - d_{15}^2\varepsilon_{11} - e_{31}^2\mu_{11},
\end{aligned}
\tag{A.8}
$$

$$
b_9 = \varepsilon_{33}\mu_{11} - 2g_{11}g_{33} + \varepsilon_{11}\mu_{33}, \tag{A.9}
$$

$$
b_{10} = c_{33}g_{33}^2 + c_{44}g_{33}^2 - c_{44}\varepsilon_{33}\mu_{33} - d_{33}^2\varepsilon_{33} - e_{33}^2\mu_{33} - c_{33}\varepsilon_{33}\mu_{33} + 2e_{33}d_{33}g_{33}, \tag{A.10}
$$

$$
b_{11} = \varepsilon_{33}\mu_{33} - g_{33}^2. \tag{A.11}
$$

Besides, the constants in Eq. (30) are given as,

$$
k_{ij} = \beta_{ij} / (\alpha_j s_j^2) \quad (i = 1, 2, 3)
$$

$$
\begin{aligned}
\omega_{1j} &= c_{44}(1 + k_{1j}) + e_{15}k_{2j} + d_{15}k_{3j}, \\
\omega_{2j} &= e_{15}(1 + k_{1j}) - \varepsilon_{11}k_{2j} - g_{11}k_{3j}, \\
\omega_{3j} &= d_{15}(1 + k_{1j}) - g_{11}k_{2j} - \mu_{11}k_{3j},
\end{aligned}
\tag{A.12}
$$

$$
\rho_1 = c_{44},\ \rho_2 = e_{15},\ \rho_3 = d_{15},
$$

where

$$
\alpha_j = -a_1 + a_2 s_j^2 - a_3 s_j^4, \tag{A.13}
$$

$$
\beta_{ij} = -a_{4i} + a_{5i}s_j^2 - a_{6i}s_j^4 + a_{7i}s_j^6 \quad (i = 1, 2, 3), \tag{A.14}
$$

with

$$
\begin{aligned}
a_1 = {} & (c_{13} + c_{44})(\varepsilon_{11}\mu_{11} - g_{11}^2) + (e_{15} + e_{31})(e_{15}\mu_{11} - g_{11}d_{15}) \\
& - (d_{15} + d_{31})(e_{15}g_{11} - \varepsilon_{11}d_{15}),
\end{aligned}
\tag{A.15}
$$

$$
\begin{aligned}
a_2 = {} & (c_{13} + c_{44})(\varepsilon_{11}\mu_{33} + \varepsilon_{33}\mu_{11} - 2g_{11}g_{33}) \\
& + (e_{15} + e_{31})(e_{15}\mu_{33} + e_{33}\mu_{11} - g_{11}d_{33} - g_{33}d_{15}) \\
& - (d_{15} + d_{31})(e_{15}g_{33} + e_{33}g_{11} - \varepsilon_{11}d_{33} - \varepsilon_{33}d_{15}),
\end{aligned}
\tag{A.16}
$$

$$
\begin{aligned}
a_3 = {} & (c_{13} + c_{44})(\varepsilon_{33}\mu_{33} - g_{33}^2) + (e_{15} + e_{31})(e_{33}\mu_{33} - g_{33}d_{33}) \\
& - (d_{15} + d_{31})(e_{33}g_{33} - \varepsilon_{33}d_{33}),
\end{aligned}
\tag{A.17}
$$

$$a_{41} = c_{11}(\varepsilon_{11}\mu_{11} - g_{11}^2), \tag{A.18}$$

$$\begin{aligned} a_{51} = {} & c_{11}(\varepsilon_{11}\mu_{33} + \varepsilon_{33}\mu_{11} - 2g_{11}g_{33}) + c_{44}(1-c^2)(\varepsilon_{11}\mu_{11} - g_{11}^2) \\ & + \mu_{11}(e_{15} + e_{31})^2 + \varepsilon_{11}(d_{15} + d_{31})^2 \\ & - 2g_{11}(e_{15} + e_{31})(d_{15} + d_{31}), \end{aligned} \tag{A.19}$$

$$\begin{aligned} a_{61} = {} & c_{11}(\varepsilon_{33}\mu_{33} - g_{33}^2) + c_{44}(1-c^2)(\varepsilon_{11}\mu_{33} + \varepsilon_{33}\mu_{11} - 2g_{11}g_{33}) \\ & + \mu_{33}(e_{15} + e_{31})^2 + \varepsilon_{33}(d_{31} + d_{15})^2 \\ & - 2g_{33}(e_{15} + e_{31})(d_{15} + d_{31}), \end{aligned} \tag{A.20}$$

$$a_{71} = c_{44}(1-c^2)(\varepsilon_{33}\mu_{33} - g_{33}^2), \tag{A.21}$$

$$a_{42} = c_{11}(e_{15}\mu_{11} - g_{11}d_{15}), \tag{A.22}$$

$$\begin{aligned} a_{52} = {} & c_{11}(e_{15}\mu_{33} + e_{33}\mu_{11} - g_{11}d_{33} - g_{33}d_{15}) \\ & + c_{44}(1-c^2)(e_{15}\mu_{11} - g_{11}d_{15}) \\ & - (e_{15} + e_{31})[\mu_{11}(c_{13} + c_{44}) + d_{15}(d_{15} + d_{31})] \\ & + (d_{15} + d_{31})[g_{11}(c_{13} + c_{44}) + e_{15}(d_{15} + d_{31})], \end{aligned} \tag{A.23}$$

$$\begin{aligned} a_{62} = {} & c_{11}(e_{33}\mu_{33} - g_{33}d_{33}) \\ & + c_{44}(1-c^2)(e_{15}\mu_{33} + e_{33}\mu_{11} - g_{11}d_{33} - g_{33}d_{15}) \\ & - (e_{15} + e_{31})[\mu_{33}(c_{13} + c_{44}) + d_{33}(d_{15} + d_{31})] \\ & + (d_{15} + d_{31})[g_{33}(c_{13} + c_{44}) + e_{33}(d_{15} + d_{31})], \end{aligned} \tag{A.24}$$

$$a_{72} = c_{44}(1-c^2)(e_{33}\mu_{33} - g_{33}d_{33}), \tag{A.25}$$

$$a_{43} = c_{11}(\varepsilon_{11}d_{15} - e_{15}g_{11}), \tag{A.26}$$

$$\begin{aligned} a_{53} = {} & c_{11}(-e_{15}g_{33} - e_{33}g_{11} + \varepsilon_{11}d_{33} + \varepsilon_{33}d_{15}) \\ & + c_{44}(1-c^2)(-e_{15}g_{11} + \varepsilon_{11}d_{15}) \\ & + (e_{15} + e_{31})[g_{11}(c_{13} + c_{44}) + d_{15}(e_{15} + e_{31})] \\ & - (d_{15} + d_{31})[\varepsilon_{11}(c_{13} + c_{44}) + e_{15}(e_{15} + e_{31})], \end{aligned} \tag{A.27}$$

$$\begin{aligned} a_{63} = {} & c_{11}(-e_{33}g_{33} + \varepsilon_{33}d_{33}) \\ & + c_{44}(1-c^2)(-e_{15}g_{33} - e_{33}g_{11} + \varepsilon_{11}d_{33} + \varepsilon_{33}d_{15}) \\ & + (e_{15} + e_{31})[g_{33}(c_{13} + c_{44}) + d_{33}(e_{15} + e_{31})] \\ & - (d_{15} + d_{31})[\varepsilon_{33}(c_{13} + c_{44}) + e_{33}(e_{15} + e_{31})], \end{aligned} \tag{A.28}$$

$$a_{73} = c_{44}(1-c^2)(-e_{33}g_{33} + \varepsilon_{33}d_{33}). \tag{A.29}$$

Appendix B

The intermediate variables in Eq. (49) are:

ACCEPTED MANUSCRIPT

$$r_j = -s_j\omega_{1j} - \rho_1 s_0 e^{-\alpha(s_j+s_0)h_t},$$
$$\bar{r}_j = s_j\omega_{1j} - \rho_1 s_0 e^{\alpha(s_j-s_0)h_t},$$
$$r_0 = \rho_1 s_0(-1-e^{-2\alpha s_0 h_t}),$$
$$j = 1,\ldots,4. \tag{B.1}$$

$$r_{ij} = s_j(k_{ij} - k_{i4}k_{3j}/k_{34}), i = 1,2,\ j = 1,2,3. \tag{B.2}$$

$$k_j = s_4 + s_j k_{3j}/k_{34},$$
$$\bar{k}_j = s_4 - s_j k_{3j}/k_{34}. \tag{B.3}$$

$$t_j^{(1)} = (s_4+s_j)\omega_{1j},\quad t_j^{(2)} = \omega_{2j} - \omega_{24}\omega_{3j}/\omega_{34},$$
$$\bar{t}_j^{(1)} = (s_4-s_j)\omega_{1j}.\quad \bar{t}_j^{(2)} = t_j^{(2)}. \tag{B.4}$$

$$t_j^{(3)} = \omega_{3j} - \omega_{34}e^{-\alpha(s_j+s_4)h_t},\quad t_j^{(4)} = -s_j\omega_{1j} - s_4\omega_{14}e^{-\alpha(s_j+s_4)h_t},$$
$$\bar{t}_j^{(3)} = \omega_{3j} - \omega_{34}e^{\alpha(s_j-s_4)h_t},\quad \bar{t}_j^{(4)} = s_j\omega_{1j} - s_4\omega_{14}e^{\alpha(s_j-s_4)h_t}, \tag{B.5}$$

$$t_{ij}^{(1)} = r_{ij}\bar{k}_3/r_{i3} + k_j,$$
$$\bar{t}_{ij}^{(1)} = -r_{ij}\bar{k}_3/r_{i3} + \bar{k}_j, \tag{B.6}$$

$$r_j^{(i)} = t_j^{(i)}\bar{k}_3/\bar{t}_3^{(i)} - k_j e^{-\alpha(s_j+s_3)h_t},$$
$$\bar{r}_j^{(i)} = \bar{t}_j^{(i)}\bar{k}_3/\bar{t}_3^{(i)} - \bar{k}_j e^{\alpha(s_j-s_3)h_t}. \tag{B.7}$$

$$s_j^{(i)} = r_j^{(i)} - \bar{r}_2^{(i)}t_{2j}^{(1)}e^{-\alpha(s_j+s_2)h_t}/\bar{t}_{22}^{(1)},$$
$$\bar{s}_1^{(i)} = \bar{r}_1^{(i)} - \bar{r}_2^{(i)}\bar{t}_{21}^{(1)}e^{\alpha(s_1-s_2)h_t}/\bar{t}_{22}^{(1)}. \tag{B.8}$$

$$s_j^{(5)} = [t_{1j}^{(1)} - \bar{t}_{12}^{(1)}t_{2j}^{(1)}/\bar{t}_{22}^{(1)}]e^{-\alpha(s_j+s_1)h_t},$$
$$\bar{s}_1^{(5)} = [\bar{t}_{11}^{(1)} - \bar{t}_{12}^{(1)}\bar{t}_{21}^{(1)}/\bar{t}_{22}^{(1)}]. \tag{B.9}$$

$$k_j^{(i)} = s_j^{(i)} - \bar{s}_1^{(i)}s_j^{(5)}/\bar{s}_1^{(5)}. \tag{B.10}$$

$$p^{(1)} = [-s_4\tilde{\tilde{p}}/\alpha^2]\bar{k}_3/\bar{t}_3^{(1)},$$
$$p^{(2)} = [\omega_{24}\tilde{\tilde{g}}/\omega_{34}/\alpha^2 - \tilde{\tilde{q}}/\alpha^2]\bar{k}_3/\bar{t}_3^{(2)},\quad l_j^{(i)} = k_j^{(i)} - k_4^{(i)}k_j^{(4)}/k_4^{(4)}. \tag{B.11}$$
$$p^{(3)} = [-\tilde{\tilde{g}}/\alpha^2]\bar{k}_3/\bar{t}_3^{(3)}.$$

ACCEPTED MANUSCRIPT

$$h_j^{(i)} = l_j^{(i)} - l_3^{(i)} l_j^{(3)} / l_3^{(3)}. \quad \begin{aligned} q^{(1)} &= p^{(1)} - p^{(3)} l_3^{(1)} / l_3^{(3)}, \\ q^{(2)} &= p^{(2)} - p^{(3)} l_3^{(2)} / l_3^{(3)}. \end{aligned} \tag{B.12}$$

References

Bonaldi, F., Geymonat, G., Krasucki, F., 2015. Modeling of smart materials with thermal effects: Dynamic and quasi-static evolution. Mathematical Models and Methods in Applied Sciences 25, 2633-2667.

Challa, V., Prasad, M., Fisher, F., 2009. A coupled piezoelectric–electromagnetic energy harvesting technique for achieving increased power output through damping matching. Smart materials and Structures 18, 095029.

Chen, W., Lee, K., Ding, H., 2004. General solution for transversely isotropic magneto-electro-thermo-elasticity and the potential theory method. International Journal of Engineering Science 42, 1361-1379.

Chen, W., Pan, E., Wang, H., Zhang, C., 2010. Theory of indentation on multiferroic composite materials. Journal of the Mechanics and Physics of Solids 58, 1524-1551.

Eerenstein, W., Mathur, N., Scott, J., 2006. Multiferroic and magnetoelectric materials. nature 442, 759.

Erturk, A., Hoffmann, J., Inman, D., 2009. A piezomagnetoelastic structure for broadband vibration energy harvesting. Applied Physics Letters 94, 254102.

Gu, L., Cui, N., Cheng, L., Xu, Q., Bai, S., Yuan, M., Wu, W., Liu, J., Zhao, Y., Ma, F., 2012. Flexible fiber nanogenerator with 209 V output voltage directly powers a light-emitting diode. Nano letters 13, 91-94.

Ding, H., 1996. General solutions for coupled equations for piezoelectric media. International Journal of Solids and Structures 33, 2283-2298.

Hu, H., 1953. On the three-dimensional problems of the theory of elasticity of a transversely isotropic body.

Hu, Y., Wang, Z., 2015. Recent progress in piezoelectric nanogenerators as a sustainable power source in self-powered systems and active sensors. Nano Energy 14, 3-14.

Kim, D., Lee, S., Lin, Z., Choi, K., Doo, S., Chang, H., Leem, J., Wang, Z., Kim, S., 2014. High temperature processed ZnO nanorods using flexible and transparent mica substrates for dye-sensitized solar cells and piezoelectric nanogenerators. Nano Energy 9, 101-111.

Kirchhof, C., Krantz, M., Teliban, I., Jahns, R., Marauska, S., Wagner, B., Knöchel, R., Gerken, M., Meyners, D., Quandt, E., 2013. Giant magnetoelectric effect in vacuum. Applied Physics Letters 102, 232905.

Kulkarni, A., Meurisch, K., Teliban, I., Jahns, R., Strunskus, T., Piorra, A., Knöchel, R., Faupel, F., 2014. Giant magnetoelectric effect at low frequencies in polymer-based thin film

composites. Applied Physics Letters 104, 022904.

Lafont, T., Gimeno, L., Delamare, J., Lebedev, G., Zakharov, D., Viala, B., Cugat, O., Galopin, N., Garbuio, L., Geoffroy, O., 2012. Magnetostrictive–piezoelectric composite structures for energy harvesting. Journal of Micromechanics and Microengineering 22, 094009.

Li, P., Gao, S., Cai, H., 2015a. Modeling and analysis of hybrid piezoelectric and electromagnetic energy harvesting from random vibrations. Microsystem Technologies 21, 401-414.

Li, X., Wu, F., Jin, X., Chen, W., 2015b. 3D coupled field in a transversely isotropic magneto-electro-elastic half space punched by an elliptic indenter. Journal of the Mechanics and Physics of Solids 75, 1-44.

Li, X., Zheng, R., Chen, W., 2014. Fundamental solutions to contact problems of a magneto-electro-elastic half-space indented by a semi-infinite punch. International Journal of Solids and Structures 51, 164-178.

Liu, B., Sun, T., He, J., Dravid, V., 2010. Sol− Gel-Derived Epitaxial Nanocomposite Thin Films with Large Sharp Magnetoelectric Effect. ACS nano 4, 6836-6842.

Liu, M., Yang, F., 2012. Finite element simulation of the effect of electric boundary conditions on the spherical indentation of transversely isotropic piezoelectric films. Smart Materials and Structures 21, 105020.

Liu, S., Hua, D., Chen, W., Wang, Q., 2007. Tribological modeling: application of fast Fourier transform. Tribology international 40, 1284-1293.

Liu, S., Jin, X., Wang, Z., Keer, L., Wang, Q., 2012. Analytical solution for elastic fields caused by eigenstrains in a half-space and numerical implementation based on FFT. International Journal of Plasticity 35, 135-154.

Liu, S., Wang, Q., 2002. Studying contact stress fields caused by surface tractions with a discrete convolution and fast Fourier transform algorithm. Journal of tribology 124, 36-45.

Liu, S., Wang, Q., Liu, G., 2000. A versatile method of discrete convolution and FFT (DC-FFT) for contact analyses. Wear 243, 101-111.

Loja, M., Soares, C., Barbosa, J., 2014. Optimization of magneto-electro-elastic composite structures using differential evolution. Composite Structures 107, 276-287.

Makagon, A., Kachanov, M., Kalinin, S., Karapetian, E., 2007. Indentation of spherical and conical punches into piezoelectric half-space with frictional sliding: applications to scanning probe microscopy. Physical Review B 76, 064115.

Makagon, A., Kachanov, M., Karapetian, E., Kalinin, S., 2009. Piezoelectric indentation of a flat circular punch accompanied by frictional sliding and applications to scanning probe microscopy. International journal of engineering science 47, 221-239.

Michopoulos, J., Young, M., Iliopoulos, A., 2015. A multiphysics theory for the static contact of deformable conductors with fractal rough surfaces. IEEE Transactions on Plasma

Science 43, 1597-1610.

Pan, E., 2001. Exact solution for simply supported and multilayered magneto-electro-elastic plates. Journal of applied Mechanics 68, 608-618.

Parton, V., Kudryavtsev, B., 1988. Electromagnetoelasticity: piezoelectrics and electrically conductive solids. Taylor & Francis.

Hou, P., Andrew, Y., Ding, H., 2003. The elliptical Hertzian contact of transversely isotropic magnetoelectroelastic bodies. International journal of solids and structures 40, 2833-2850.

Polonsky, I., Keer, L., 1999. A numerical method for solving rough contact problems based on the multi-level multi-summation and conjugate gradient techniques. Wear 231, 206-219.

Ramesh, R., Spaldin, N., 2007. Multiferroics: progress and prospects in thin films. Nature materials 6, 21.

Rodríguez-Tembleque, L., Buroni, F., Sáez, A., Aliabadi, M., 2016a. 3D coupled multifield magneto-electro-elastic contact modelling. International Journal of Mechanical Sciences 114, 35-51.

Rodríguez-Tembleque, L., Sáez, A., Aliabadi, M., 2016b. Indentation response of piezoelectric films under frictional contact. International Journal of Engineering Science 107, 36-53.

Shan, X., Guan, S., Liu, Z., Xu, Z., Xie, T., 2013. A new energy harvester using a piezoelectric and suspension electromagnetic mechanism. Journal of Zhejiang University SCIENCE A 14, 890-897.

Sladek, J., Sladek, V., Solek, P., Zhang, C., 2010. Fracture analysis in continuously nonhomogeneous magneto-electro-elastic solids under a thermal load by the MLPG. International Journal of Solids and Structures 47, 1381-1391.

Sodano, H., Inman, D., Park, G., 2004. A review of power harvesting from vibration using piezoelectric materials. Shock and Vibration Digest 36, 197-206.

Sun, K., Kim, Y., 2010. Layout design optimization for magneto-electro-elastic laminate composites for maximized energy conversion under mechanical loading. Smart Materials and Structures 19, 055008.

Umeda, M., Nakamura, K., Ueha, S., 1996. Analysis of the transformation of mechanical impact energy to electric energy using piezoelectric vibrator. Japanese Journal of Applied Physics 35, 3267.

Umeda, M., Nakamura, K., Ueha, S., 1997. Energy storage characteristics of a piezo-generator using impact induced vibration. Japanese journal of applied physics 36, 3146.

Vopson, M., 2015. Fundamentals of multiferroic materials and their possible applications. Critical Reviews in Solid State and Materials Sciences 40, 223-250.

Wang, C., Liao, W., Lin, Z., Ku, N., Li, Y., Chen, Y., Wang, Z., Liu, C., 2014. Optimization of the

output efficiency of GaN nanowire piezoelectric nanogenerators by tuning the free carrier concentration. Advanced Energy Materials 4.

Wang, J., Chen, C., 2011. Indentation responses of piezoelectric films ideally bonded to an elastic substrate. International Journal of Solids and Structures 48, 2743-2754.

Wang, J., Chen, C., Lu, T., 2008. Indentation responses of piezoelectric films. Journal of the Mechanics and Physics of Solids 56, 3331-3351.

Wang, L., Yuan, F., 2008. Vibration energy harvesting by magnetostrictive material. Smart Materials and Structures 17, 045009.

Wang, Y., Hu, J., Lin, Y., Nan, C., 2010. Multiferroic magnetoelectric composite nanostructures. NPG Asia Materials 2, 61.

Wang, Z., Wang, W., Meng, F., Wang, J., 2011. Fretting contact analysis on three-dimensional elastic layered half space. Journal of Tribology 133, 031401.

Wang, Z., Jin, X., Liu, S., Keer, L., Cao, J., Wang, Q., 2013. A new fast method for solving contact plasticity and its application in analyzing elasto-plastic partial slip. Mechanics of Materials 60, 18-35.

Wang, Z., Yu, C., Wang, Q., 2015. An efficient method for solving three-dimensional fretting contact problems involving multilayered or functionally graded materials. International Journal of Solids and Structures 66, 46-61.

Wang, Z., Song, J., 2006. Piezoelectric nanogenerators based on zinc oxide nanowire arrays. Science 312, 242-246.

Webster, M., Sayles, R., 1986. A numerical model for the elastic frictionless contact of real rough surfaces. Journal of tribology 108, 314-320.

Xu, Q., Qin, Y., 2017. Theoretical study of enhancing the piezoelectric nanogenerator's output power by optimizing the external force's shape. APL Materials 5, 074101.

Yu, C., Wang, Z., Wang, Q., 2014. Analytical frequency response functions for contact of multilayered materials. Mechanics of Materials 76, 102-120.

Zhang, X., Shen, H., Liu, J., Deng, S., Li, X., Cai, Z., Zhu, M., 2015. An efficient numerical model for predicting the torsional fretting wear considering real rough surface. Wear 344, 32-45.

Zhang, X., Wang, Z., Shen, H., Wang, Q., 2017. Frictional contact involving a multiferroic thin film subjected to surface magnetoelectroelastic effects. International Journal of Mechanical Sciences 131, 633-648.

Zhang, X., Wang, Z., Shen, H., Wang, Q., 2018. An efficient model for the frictional contact between two multiferroic bodies. International Journal of Solids and Structures 130, 133-152.

Zheng, B., Chang, C., Gea, H., 2009. Topology optimization of energy harvesting devices using piezoelectric materials. Structural and Multidisciplinary Optimization 38, 17-23.

Zhou, Q., Wang, J., Wan, Q., Jin, F., Yang, W., Miao, Q., Wang, Z., 2017. Numerical analysis of

ACCEPTED MANUSCRIPT

the influence of distributed inhomogeneities on tangential fretting. Proceedings of the Institution of Mechanical Engineers, Part J: Journal of Engineering Tribology 231, 1350-1370.

Zhou, Y., Kim, T., 2015. Dynamic contact modeling of anisotropic magneto-electro-elastic materials with volume fraction changes. Composite Structures 131, 1099-1110.

Zhou, Y., Lee, K., 2012a. Contact problem for magneto-electro-elastic half-plane materials indented by a moving punch. Part I: Closed-form solutions. International Journal of Solids and Structures 49, 3853-3865.

Zhou, Y., Lee, K., 2012b. Contact problem for magneto-electro-elastic half-plane materials indented by a moving punch. Part II: numerical results. International Journal of Solids and Structures 49, 3866-3882.

Zhou, Y., Lee, K., 2013. Theory of sliding contact for multiferroic materials indented by a rigid punch. International Journal of Mechanical Sciences 66, 156-167.

Zhou, Y., Liu, W., Huang, X., Zhang, A., Zhang, Y., Wang, Z., 2016. Theoretical study on two-dimensional MoS 2 piezoelectric nanogenerators. Nano Research 9, 800-807.

Zucca, M., Bottauscio, O., Beatrice, C., Fiorillo, F., 2011. Modeling amorphous ribbons in energy harvesting applications. IEEE Transactions on Magnetics 47, 4421-4424.

ACCEPTED MANUSCRIPT